

**NAM**

# **Dynamic modelling of large tremors in the Groningen field using extended seismic sources**

---

**Shell Global Solutions**

**H.M. Wentinck**

Datum August 2018

Editors Jan van Elk, & Dirk Doornhof



## General Introduction

The Huizinge earthquake of 16<sup>th</sup> August 2012 with a magnitude of  $M_L = 3.6$  had a profound impact on the Groningen community and led to the acceleration of the research program into induced seismicity in Groningen. As part of this program new capabilities were developed. For instance, geomechanical modelling of rupture processes taking place in the depleted gas reservoir of the Rotliegend formation was improved.

Using these capabilities, the Huizinge earthquake of 2012 was revisited (Ref. 1 and 2). In a previous report the same techniques are used to study the more recent Zeerijp ( $M_L = 3.4$ ) earthquake of 8<sup>th</sup> January 2018 (Ref. 3, 4).

The network of geophones and accelerometers installed in the Groningen field has been significantly expanded since the Huizinge earthquake. For the Zeerijp earthquake much more recordings are therefore available than for the Huizinge earthquake. Furthermore, methods to image the faults in the area and for estimating the hypocenter of earthquakes have also been further developed. This allows the fault hosting this earthquake to be determined with more precision.

In this report dynamic rupture modelling is applied to model the rupture on the fault identified as having hosted the rupture (as identified in reference 3).

## References

1. Kinematic modelling of large tremors in the Groningen field using extended seismic sources – Part 1, H.M. Wentinck, August 2017
2. Kinematic modelling of large tremors in the Groningen field using extended seismic sources – Part 2, H.M. Wentinck, July 2018
3. Kinematic modelling of large tremors in the Groningen field using extended seismic sources - First results related to the Zeerijp tremor ML 3.4, Shell Global Solutions, H.M. Wentinck, August 2018
4. Special Report on the Zeerijp Earthquake – 8<sup>th</sup> January 2018, NAM, Taco den Bezemer and Jan van Elk.



**NAM**

<b>Title</b>	<b>Dynamic modelling of large tremors in the Groningen field using extended seismic sources</b>		<b>Date</b>	August 2018
			<b>Initiator</b>	NAM
<b>Author(s)</b>	H.M. Wentinck	<b>Editor</b>	Jan van Elk and Dirk Doornhof	
<b>Organisation</b>	Shell Global Solutions	<b>Organisation</b>	NAM	
<b>Place in the Study and Data Acquisition Plan</b>	<p><u>Study Theme: Geomechanical Modelling</u></p> <p><u>Comment:</u></p> <p>The Huizinge earthquake of 16<sup>th</sup> August 2012 with a magnitude of <math>M_L = 3.6</math> had a profound impact on the Groningen community and led to the acceleration of the research program into induced seismicity in Groningen. As part of this program new capabilities were developed. For instance, geomechanical modelling of rupture processes taking place in the depleted gas reservoir of the Rotliegend formation was improved. Using these capabilities, the Huizinge earthquake of 2012 was revisited. In a previous report the same techniques are used to study the more recent Zeerijp (<math>M_L = 3.4</math>) earthquake of 8<sup>th</sup> January 2018.</p> <p>The network of geophones and accelerometers installed in the Groningen field has been significantly expanded since the Huizinge earthquake. For the Zeerijp earthquake much more recordings are therefore available than for the Huizinge earthquake. Furthermore, methods to image the faults in the area and to estimating the earthquake hypocenters have also been further developed. This allows the fault hosting this earthquake to be determined with more precision.</p> <p>In this report dynamic rupture modelling is applied to model the rupture on the fault identified as having hosted the rupture (as identified in a previous report).</p>			
<b>Directly linked research</b>	<ol style="list-style-type: none"> <li>1. Reservoir engineering studies in the pressure depletion for different production scenarios.</li> <li>2. Seismic monitoring activities; both the extension of the geophone network and the installation on geophones in deep wells.</li> <li>3. Geomechanical studies</li> <li>4. Subsidence and compaction studies.</li> </ol>			5.
<b>Used data</b>	KNMI Earthquake catalogue Geological maps of faults in the Rotliegend reservoir			
<b>Associated organisation</b>	Shell Global Solutions			
<b>Assurance</b>				

report for NAM 2018

Dynamic rupture modelling

Zeerijp tremor  $M_L$  3.4 in the Groningen field

by

H.M. Wentinck

Copyright Shell Global Solutions International B.V., Rijswijk International, B.V., 2018.

Neither the whole nor any part of this document may be reproduced, stored in any retrieval system or transmitted in any form or by any means (electronic, mechanical, reprographic, recording or otherwise) without the prior written consent of the copyright owner.

## Executive Summary

Dynamic rupture modelling is applied to model the rupture on the mFS7-Fault-54 fault in the Zeerijp region in the Groningen gas field. Part of this fault slipped in January 2018 and caused the Zeerijp  $M_L$  3.4 tremor.

The non-uniform reservoir rock around the fault is modelled from well logs around the Zeerijp tremor epicentre. In addition, pressure diffusion into the Carboniferous underburden is included in the calculation of the stress on the fault during gas production.

The fault has a relatively little throw of 40 m when compared to the reservoir thickness of 270 m and has a dip angle of about  $80^\circ$ . The shear stress on the fault increases with several MPa due to gas production. This increase is comparable with the shear stress before gas production and evolving from the difference between the vertical and horizontal field stresses. So far, we have disregarded other tectonic forces we are not aware of.

The analysis of the ground motions of this tremor has indicated that the slip direction of the hanging wall is primarily downwards along fault dip and that the slip plane area is relatively small for this tremor magnitude. The slip direction indicates that stresses on the fault due to the difference between the vertical and horizontal field stresses and due to gas production dominate. The moderate size of the slip plane implies that the breakdown stress drop over the slip plane during the rupture and the slip, required to release a  $M_L$  3.4 tremor, are considerable. Dynamic rupture modelling shows that such a stress drop can only be achieved when the dynamic (or residual) friction during slip is relatively low compared to the static friction on the fault plane.

The residual friction of the rock in the Carboniferous underburden determines how far the rupture can penetrate into this formation. So far, there is no observational evidence that the rupture penetrated substantially into the Carboniferous.

If the residual friction in the Carboniferous would be the same as in the reservoir, substantial rupture penetration would be possible pending on the shear stress on the fault plane and pressure diffusion into the Carboniferous. Pressure diffusion has a significant effect on the normal and shear stresses on this part of the fault.

# Table of Contents

<b>1</b>	<b>Introduction</b>	<b>4</b>
<b>2</b>	<b>Model input</b>	<b>6</b>
2.1	Seismic data . . . . .	6
2.2	Subsurface geometry, reservoir pressure and field stress . . . . .	8
2.3	Well logs and rock properties . . . . .	14
2.4	Input for constitutive models for rock failure and seismic slip . . . . .	18
2.5	Input parameters for pressure diffusion in the Carboniferous . . . . .	21
<b>3</b>	<b>Results</b>	<b>22</b>
3.1	Set-up of simulations . . . . .	22
3.2	Results . . . . .	24
<b>4</b>	<b>Discussion</b>	<b>29</b>
<b>5</b>	<b>Acknowledgements</b>	<b>31</b>
	<b>APPENDICES</b>	<b>35</b>
<b>A</b>	<b>Correlation between porosity and uniaxial compaction coefficient</b>	<b>36</b>
<b>B</b>	<b>Constitutive models for fault failure</b>	<b>42</b>
B.1	Stresses on the fault plane . . . . .	43
B.2	Linear strain weakening model . . . . .	45
B.3	Ohnaka's model . . . . .	46
B.4	Creep in the fault gouge . . . . .	47
B.5	Mapping displacements from one fault surface to the second fault surface on the other side of the fault zone . . . . .	48
<b>C</b>	<b>Breakdown stress drop</b>	<b>50</b>
C.1	Breakdown stress drop . . . . .	50

<b>D Other simulation results</b>	<b>53</b>
D.1 Additional results of simulation A . . . . .	53
D.2 Results of simulation B . . . . .	60
D.3 Source time functions . . . . .	63
D.4 Dynamic rupture simulation in three dimensions . . . . .	67

Table 0.1 : List of frequently used symbols

Symbol	Property	Unit
$c, c'$	constant	-
$C_m$	uniaxial compaction coefficient	1/Pa
$C'_m$	apparent uniaxial compaction coefficient	1/Pa
$D$	average or local slip or relative displacement at a fault plane	m
$D_c$	critical breakdown slip or critical breakdown relative displacement	m
$D_{p,cb}$	pressure diffusion constant	m <sup>2</sup> /s
$e$	unit vector	-
$E$	Young modulus	Pa
$E'_{flt}$	stiffness of the fault zone in normal direction to the fault plane	[Pa/m]
$f$	force	N
$f$	frequency	Hz
$f_c$	corner frequency	Hz
$G$	shear modulus (also the symbol $\mu$ is used)	Pa
$G'_{flt}$	stiffness of the fault zone in tangential direction to the fault plane	[Pa/m]
$h$	reservoir thickness	m
$i$	take-off angle of the ray from the source to the receiver	degree/radian
$l$	unit vector in slip direction	-
$k$	permeability	m <sup>2</sup>
$K$	bulk modulus	Pa
$K_s$	bulk modulus of the grains in the rock	Pa
$L$	length of the fault, here the dimension along fault strike	m
$L_c$	characteristic rupture dimension	m
$M$	moment magnitude	Richter
$M_L$	local magnitude	Richter
$M_0$	seismic moment	J
$n$	unit vector normal to the slip plane	-
$p$	reservoir pressure	m
$r$	distance between source and receiver	m
$S$	surface area of slip plane or slip patch	m <sup>2</sup>
$S$	dimensionless stress parameterslip patch	m <sup>2</sup>
$t$	time	s
$t_R$	duration of the rupture in the slip plane	s
$u$	displacement vector with components $(u, v, w)$	m
$V_{slip}$	mean slip velocity over the fault plane	m/s
$V_p$	velocity of primary wave	m/s
$V_s$	velocity of secondary wave	m/s
$V_r$	rupture velocity	m/s
$w_{flt}$	width of the fault zone normal to the fault plane	m
$W$	width of the fault plane, dimension along fault dip	m
$W$	parameter for the size of the nucleation patch for fault instability	Pa/m
$z$	depth	m

Table 0.2 : List of frequently used symbols, continued

Symbol	Property	Unit
$\alpha$	Biot constant	-
$\alpha$	parameter in Ohnaka's constitutive equation for fault failure	-
$\beta$	parameter in Ohnaka's constitutive equation for fault failure	-
$\gamma_h$	stress path coefficient relating changes in hor. stress and pressure	-
$\delta$	dip angle of fault	degree/radian
$\delta$	small difference	-
$\Delta$	large difference	-
$\Delta\tau$	breakdown stress drop	Pa
$\Delta t_{50}$	period in which the source time function exceeds 50% of max. value	s
$\epsilon_z$	strain along depth, in the z-direction	m/m
$\eta$	parameter in Ohnaka's constitutive equation for fault failure	-
$\theta$	angle the normal of the fault plane makes with the horizon	degree/radian
$\theta$	angle between line from tremor epicentre to receiver and fault strike	degree/radian
$\kappa_f$	fluid compressibility	Pa <sup>-1</sup>
$\lambda$	first Lamé parameter	Pa
$\lambda$	rake angle of slip vector	degree/radian
$\mu$	shear modulus of rock or second Lamé parameter	Pa
$\mu$	friction coefficient	-
$\mu_f$	fluid viscosity	Pa.s
$\nu$	Poisson ratio	Pa
$\rho$	mass density of rock	kg/m <sup>3</sup>
$\sigma_n$	normal stress	Pa
$\tau$	shear stress	Pa
$\tau$	typical time	s
$\tau_r$	rise time in source time function	s
$\phi$	porosity	-
$\phi$	fault strike azimuth angle with respect to the north direction	degree/radian
$\phi_s$	source-receiver azimuth angle with respect to the north direction	degree/radian
$\omega$	angular frequency	rad/s
$\omega_c$	radial or angular corner frequency	rad/s

Table 0.3 : List of frequently used symbols, continued

Symbol	Refers to
.....	.....
subscripts	
an	Anhydrite formation
cb	Carboniferous formation
f	fluid
flt	fault plane or fault zone
geom	geometric
l	left to the fault plane
n	normal to the fault plane
ob	overburden
p	P wave
r	right to the fault plane
r	rupture
rs	reservoir
s	S wave
t	tangential to the fault plane
zs	Zechstein formation
superscripts	
p	P wave
s	S wave
abbreviations	
DSS	distributed strain sensing
EBN	Energie Beheer Nederland
FEM	finite element method
KNMI	Koninklijk Nederlands Meteorologisch Instituut
NAM	Nederlandse Aardolie Maatschappij
RTCiM	rate-type isotach compaction model
SGS-I	Shell Global Solutions International

# Chapter 1

## Introduction

Currently, the hypocentres and focal mechanisms of tremors generated in the Groningen field are determined on a regular basis from ground displacements recorded by the extensive network of seismometers in the Groningen field. Using convenient inversion methods, this is done by KNMI, ExxonMobil and SGS-I. To understand these tremors in terms of geomechanical stresses and mechanical rock properties, this report combines the results of dynamic rupture modelling and seismic data for a recent relatively large tremor. This tremor is the Zeerijp tremor of 8 January 2018 with a local magnitude  $M_L$  3.4.

Detailed information is available about the properties and dimensions of the reservoir and the formations above it, including those from three well logs in the reservoir in this region of the Groningen field. The dip and strike azimuth angles of the fault on which the rupture took place have been determined from ant-tracking and in one of the wells uniaxial strain in the reservoir following from compaction due to gas production has been measured recently over a period of about 18 months using a distributed optical fibre cable. The measured strain in the reservoir is in good agreement with the reservoir compaction data derived from subsidence measurements. All this data has been used to constrain the input parameters for dynamic rupture modelling.

The analysis of the ground motions following from the Zeerijp tremor, indicates that the slip direction of the hanging wall is primarily downwards along fault dip. This slip direction indicates that stresses on the fault due to the difference between vertical and horizontal field stresses and due to gas production dominate.

The analysis of the corner frequencies of the ground motion spectra and the apparent source time functions of the Zeerijp tremor indicate that the largest dimension of the slip plane is less than 0.4 km and that the slip area is substantially less than 1 km<sup>2</sup>, see Wentinck (2018a). The moderate size of the slip plane and the slip required for a  $M_L$  3.4 tremor imply that the breakdown stress drop  $\Delta\tau$  [Pa] must be considerable as the tremor magnitude is proportional to the slip surface area  $S$  [m<sup>2</sup>] and to  $\Delta\tau$ , see Appendix C.

From a geomechanical viewpoint, the breakdown stress drop primarily depends on the

brittleness of the rock and the stress on the fault plane over which slip takes place. To a lesser extent, it depends on fault plane roughness and variations in rock properties along the fault plane.

The input parameters and the constitutive model for the brittleness of the rock determine the fault slip dynamics. In this work we have used Ohnaka's constitutive model, see Ohnaka (2013). It calculates the frictional resistance along the fault plane as a function of the relative displacement  $D$  [m] between two surfaces on both sides of the fault plane. The main input parameters are the static and dynamic friction coefficients  $\mu_s$  and  $\mu_r$  [-] and the so-called critical breakdown relative displacement (or critical breakdown slip)  $D_c$  [m]. The friction coefficient decreases from the static to the dynamic value over a slip distance of about  $D_c$ .

The values of the input parameters are constrained by work on natural earthquakes and by friction experiments in the laboratory. To constrain them more for a specific case, such as for the Rotliegend sandstone reservoir rock and the Carboniferous underburden of the Groningen field, additional experiments are required, see Chapter 4.

Currently, we have the computational capabilities to perform three-dimensional dynamic rupture simulations on rough fault planes in non-uniform rock and under an inhomogeneous loading, as for example follows from reservoir compaction by gas production. For the purpose of this work we show only results of two dimensional simulations on a smooth fault. These results show that the required breakdown stress drop can only be achieved when the dynamic (or residual) friction during slip is relatively low compared to the static friction on the fault plane.

Adding to similar work done by Buijze et al. (2015), van den Bogert (2018b) and van den Bogert (2018a), this work includes non-uniform rock properties in the reservoir over depth, the use of Ohnaka's constitutive model and a plausible pressure depletion profile in the upper part of the Carboniferous formation due to pressure diffusion. The pressure depletion profile is important in relation rupture penetration into the Carboniferous. So far, the pressure profile in the Carboniferous is poorly constrained because of uncertainty about the permeability of the Carboniferous rock.

Chapter 2 presents field data and other input data used in the simulations. Chapter 3 shows the simulation results and is followed by a discussion in Chapter 4. Appendix A shows the equations used for correlations between porosity and mechanical rock properties. Appendix B shows the equations of the constitutive models used. Appendix C shows some expressions for the breakdown stress drop and Appendix D shows more results of simulations.

# Chapter 2

## Model input

The input data for dynamic rupture modelling are the geometry of the subsurface formations and the mFS7-Fault-54 fault, the field stress in this region of the Groningen field, the geomechanical properties of the rock around the fault as derived from well logs and seismic data and the constitutive model determining fault failure.

### 2.1 Seismic data

According to seismic moment tensor inversions by Bernard Dost (KNMI) and Ewoud van Dedem (SGS-I), the tremor epicentre coordinates of the Zeerijp  $M_L$  3.4 tremor are  $X = 245714$  m and  $Y = 597574$  m and  $X = 245600$  m and  $Y = 597600$  m, respectively<sup>1</sup>. The tremor hypocentre is located in the reservoir at a depth of about 2950 m and on fault mFS7-Fault-54<sup>2</sup>. Figure 2.1 shows a map of this fault and others in this region, the Zeerijp  $M_L$  3.4 tremor epicentre and the locations of the seismometer stations used.

The moment tensor derived from the ground motions of this tremor can be decomposed as a double couple, or in other words, as a predominant tangential slip along a fault plane. The strike azimuth of the slip plane is  $\phi \sim 310^\circ$ . The dip angle of the slip plane is  $\delta \sim 67^\circ$ . The slip direction of the hanging wall is predominantly downwards suggesting that the contribution of stress build-up in a direction along fault strike is less important. Hence, we disregard in this model a significant shear stress in fault strike direction.

An insignificant shear stress along fault strike would agree with the typical orientation of the maximum and minimum horizontal field stresses in the Groningen field. According to van Eijs and Valencia (2013), Figure 11, the maximum horizontal stress is between NW-SE and N-S direction and, consequently, the minimum horizontal stress is between the NE-SW and W-E direction. So, the minimum horizontal stress is in the direction of

---

<sup>1</sup>X and Y are coordinates of the Dutch Rijksdriehoeksstelsel coordinate system.

<sup>2</sup>The fault strike azimuth angle  $\phi$  is defined as the angle between the Earth north direction and the fault strike where it is measured clockwise round from north.

the normal azimuth angle of fault mFS7-Fault-54<sup>3</sup>.

The corner frequencies in the spectra of the ground displacements recorded by seismometer stations near the tremor epicentre and apparent source time functions for the Zeerijp tremor indicate that the area of the slip plane is considerably less than 1 km<sup>2</sup>, see Wentinck (2018a). For a tremor with a magnitude  $M = 3.4$ , this means that the breakdown stress drop is relatively high, i.e, 3 - 5 MPa, see Appendix C.

---

<sup>3</sup>The fault normal azimuth angle (to the hanging wall) is 90° clockwise with respect to the fault strike azimuth angle. In this case, it is about 50° with respect to the north in clockwise direction.

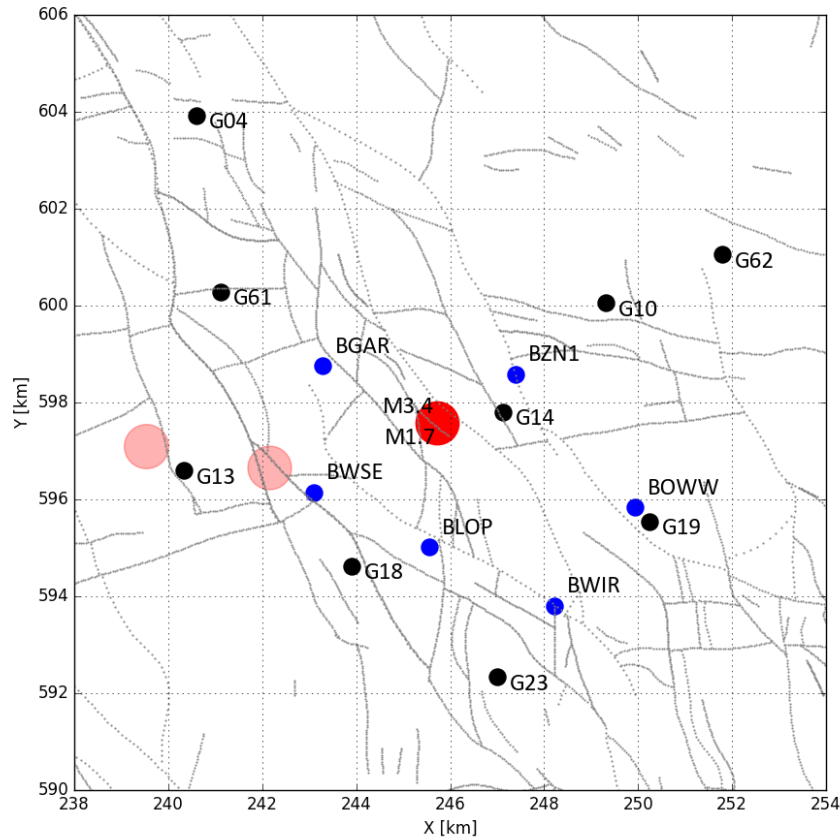


Figure 2.1 : Faults and locations of the epicentre of the Zeerijp  $M_L$  3.4 tremor and the seismometer stations used.

The thin grey dotted and solid lines are intersections of the faults with the top horizon of the Rotliegend reservoir according to the NAM fault database. This database is primarily used for reservoir flow models and for geomechanical calculations.

The red dot shows the location of the  $M_L$  3.4 tremor. The two pink dots show the epicentres of the Huizinge 2012  $M_L$  3.4 (left) and Westeremden 2006  $M_L$  3.5 (centre) tremors. The blue and black dots show the ground accelerometers and shallow boreholes operated by KNMI, respectively. The latter have 4 geophones in the borehole at 50, 100, 150 and 200 m depth and an accelerometer on the surface, see also Wentinck (2018a).

## 2.2 Subsurface geometry, reservoir pressure and field stress

The epicentre of the Zeerijp tremor is on fault mFS7-Fault-54. According to the NAM fault database for reservoir modelling and geomechanics, the fault strike azimuth and

fault dip angles of the mFS7-Fault-54 fault near the tremor hypocentre are  $\phi \sim 315 \pm 10^\circ$  and  $\delta \sim 80 \pm 3^\circ$ , respectively. The fault throw near the tremor hypocentre is about 40 m. The fault strike azimuth corresponds quite well with the one derived from seismic moment tensor inversions by Bernard Dost (KNMI) and Ewoud van Dedem (SGS-I). The fault is dipping to the east.

The correspondence is less good for the dip angle of the fault  $\delta$ . Bernard Dost (KNMI) and Ewoud van Dedem (SGS-I) derive  $\delta \sim 67^\circ$ . On the other hand, Alan Wood (SGS-I) derives from ant-tracking, a dip angle in the range  $75 - 80^\circ$  in agreement with the NAM fault database, see Figure 2.3 . Around the tremor hypocentre, the fault is quite smooth along dip but less smooth along fault strike.

According to ant-tracking results of Marloes Kortekaas (EBN), the structure of fault mFS7-Fault-54 around the Zeerijp tremor hypocentre seems more complicated, see Figures 2.2 and 2.3 . A reverse and a normal fault join around the tremor hypocentre. The hypocentre is on a minor fault. The ant-tracking of the fault is clear at the top of the reservoir but becomes in the reservoir less clear. The broken fault on the right side dips to the east. Regarding the seismic moment tensor results, we disregard in this report the reverse fault on the left side in the dynamic rupture modelling.

From seismic horizons between the subsurface formations according to the seismic velocity model of NAM 2015, in an area of a few square km around the epicentre of the Zeerijp tremor, the mean depth of the horizon between the Zechstein<sup>4</sup> and Trias is 1965 m, between the anhydrite and the Zechstein is 2801 m, between the reservoir and the anhydrite formation is 2852 m and between the Carboniferous and the reservoir is 3120 m.

Modelling a fault with a throw of 40 m, the horizons between the formations on the left side of the fault are shifted 20 m up with respect to the mean values. At the right side of the fault, they are shifted 20 m down with respect to the mean values.

Before the start of the gas production, the reservoir pressure  $p$  [Pa] in the main part of the Groningen field is about 35 MPa. The reservoir pressure in the Zeerijp region of the field in January 2018 can be estimated from reservoir modelling<sup>5</sup>. We use  $p \sim 9$  MPa. In addition, we assume that the reservoir pressure is uniform and equal on both sides of

<sup>4</sup>The lower Zechstein, floater and upper Zechstein are combined to form one formation. The anhydrite layer is explicitly included in the model because it has distinct different mechanical properties than the lower Zechstein and is on top of the reservoir, see §2.3.

<sup>5</sup>According to a history match from reservoir modelling by Leendert Geurtsen (NAM), the reservoir pressure in the Zeerijp 1 well at 1 January 2017 is  $p \sim 9.6$  MPa. In the Zeerijp 2 well in December 2014,  $p \sim 10$  MPa. In the Zeerijp 3 well in August 2015,  $p \sim 9.3$  MPa.

The reservoir pressure reduction in this region of the Groningen field over the last five years is about 0.4 MPa/year. On the other hand, according to Cannon and Kole (2016), Figure 4.27, the modelled pressure depletion at the ZRP-3 well location is in a period of about 8 months in 2016 about 0.13 MPa, equivalent to 0.2 MPa/year. Extrapolation of the reservoir pressure to January 2018 using a pressure reduction rate of 0.3 MPa/year: in the Zeerijp 1 well,  $p \sim 9.3$  MPa, in the Zeerijp 2 well,  $p \sim 9.0$  MPa and in the Zeerijp 3a well,  $p \sim 9.0$  MPa.

the fault.

According to van Eijs and Valencia (2013), Figure 1, thirteen wells have been investigated to show a variation of the mean vertical stress gradient between 0.0219 and 0.0235 MPa/m at a reference level of 3 km depth. The difference in vertical stress gradients is mainly caused by variations in the Zechstein salt thickness. The higher values apply for regions where the Zechstein is thin. For the Zeerijp region, a vertical stress gradient of 0.022 MPa/m applies. At a depth of 3 km, the vertical stress is 68 MPa.

According to these authors, the horizontal stresses in the Groningen field are poorly constrained by data. Data points reflecting a possible value for the minimum horizontal stress at the start of the gas production and later are limited and values for the field virgin stress value and the so-called stress path coefficient  $\gamma_h \equiv \Delta\sigma_h/\Delta p$ , relating the change in the horizontal stress  $\Delta\sigma_h$  [Pa] and the change in the reservoir pressure  $\Delta p$  [Pa], can hardly be extracted from these three data points. Furthermore, it is likely that the value of these parameters significantly vary over the field.

The limited data suggests  $\gamma_h = 0.43$ . This value is quite lower than a value following from a theoretical expression for poro-elastic media, i.e.,  $\gamma_h = \alpha(1 - 2\nu)/(1 - \nu)$  where  $\alpha$  is the Biot constant and  $\nu$  the Poisson ratio of the reservoir rock. For typical values,  $\nu = 0.25$  and  $\alpha = 0.8$ , we have  $\gamma_h = 0.8 \times 0.5/0.75 = 0.53$ . For  $\nu = 0.2$ ,  $\gamma_h = 0.6$ <sup>6</sup>

Following Sanz et al. (2015) and van den Bogert (2018b), we use for gradient of the minimum horizontal stress 0.016 MPa/m. At a depth of 3 km, the minimum horizontal stress is 48 MPa. Table 2.1 shows the input parameters used to define the subsurface geometry and field stresses.

---

<sup>6</sup>According to van Eijs and Valencia (2013), a full logging program over the open hole section of the water injection well Borgsweer-5, drilled in 2013 in the eastern part of the Groningen field, two out of two cycles of a so-called minifrac test gave a value of 39.5 MPa for the fracture closure pressure for a depletion of 15 MPa was measured (report van der Bas, 2013). For  $\gamma_h = 0.5$ , the virgin minimal horizontal stress would have been  $39.5 + 0.5 \times 15 = 46$  MPa.

Table 2.1 : Input parameters for the model related to the subsurface geometry, reservoir pressure and stress on the fault.

Property	unit	value
.....	.....	.....
geometry		
mean depth of centre of reservoir	m	2986
thickness of overburden	m	1945
thickness of Zechstein	m	836
thickness of anhydrite formation	m	50
thickness of reservoir	m	268
thickness of Carboniferous underburden	m	2872
fault dip	degrees	80
gas pressure in reservoir before compaction	MPa	35
gas pressure in reservoir during rupture	MPa	9
gradient for vertical stress	MPa/m	0.022
gradient for minimum horizontal stress	MPa/m	0.016
gradient for hydrostatic pressure outside the reservoir	MPa/m	0.011
gradient for hydrostatic pressure inside the reservoir before compaction	MPa/m	0.0015
vertical field stress in centre of reservoir	MPa	68
horizontal field stress in centre of reservoir	MPa	48

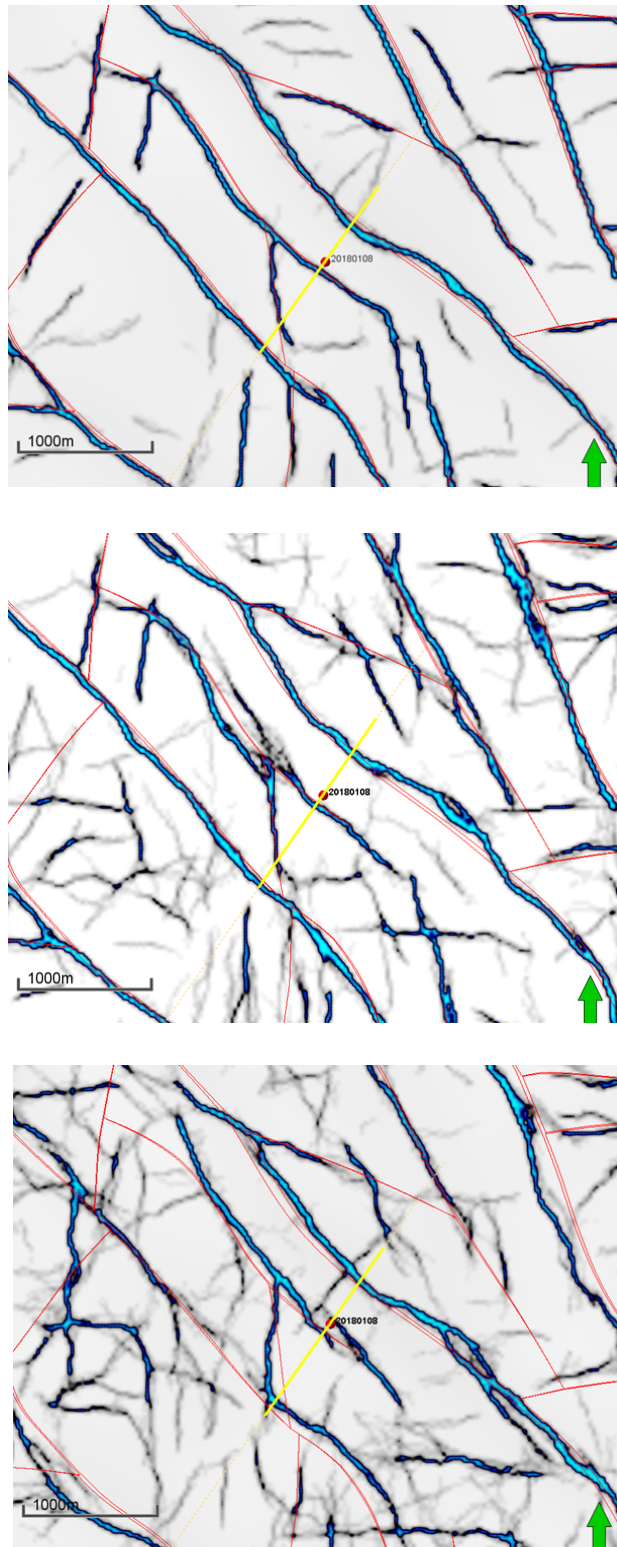
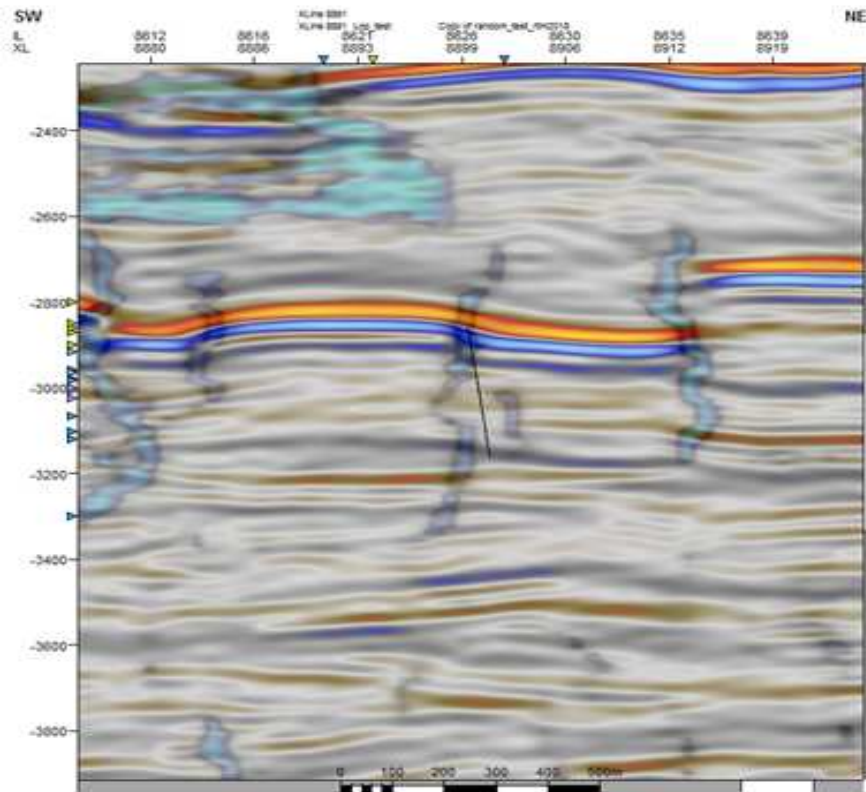


Figure 2.2 : Faults derived from ant-tracking faults using Petrel<sup>TM</sup> on the seismic data cube of 2015 of the Groningen field by Marloes Kortekaas (EBN). From top to bottom, the figures show planes at the depth of the top of the reservoir, at the depth of the tremor hypocentre and at the depth of the bottom of the reservoir. Near the tremor hypocentre there may be a fault jog, i.e., an overstep or a bend that connects two sub-parallel but non-collinear portions of a fault zone.

The red dot shows the tremor hypocentre with RD coordinates  $X = 245714$  m,  $Y = 597574$  m and  $Z = -2950$  m. The thin red lines show faults according to the NAM fault database.



## 2.3 Well logs and rock properties

In general, the uniaxial compaction coefficient and Poisson ratio of the reservoir rock depends on various parameters, such as the grain size, clay content, cementation between the grains, etc.. For a recent overview of mechanical properties of the Rotliegend sandstone in the Groningen field, see Hol et al. (2018). In this report, we only consider a variation of the uniaxial compaction coefficient with porosity.

Figure 2.4 shows a map of the mean porosity of the reservoir in the region around the Zeerijp epicentre and the locations of the tremor epicentre and the Zeerijp 1, 2 and 3a wells for which well logs are available. In particular, the well log of the Zeerijp 3a well has been used to derive the rock properties over the depth of the reservoir. Figure A.1 in Appendix A shows the porosity profiles in the Zeerijp 1, 2 and 3a wells. They are quite comparable and show that the reservoir is non-uniform. In the upper 80 m of the reservoir the porosity is above 20%, in the lower part it is about 17%.

Figure 2.5 shows the profile of the porosity as has been measured in the Zeerijp 3a well and the calculated uniaxial compaction coefficient  $C_m$  [1/Pa] versus the reservoir depth.  $C_m$  is calculated from an empirical correlation using the so-called RTCiM model<sup>7</sup> between the porosity  $\phi$  [-] and the uniaxial compaction coefficient  $C_m$  [Pa<sup>-1</sup>]. The latter is derived from compaction data calculated from subsidence measurements in the Groningen field. The empirical correlation used is explained in Appendix A and is shown in Figure A.4 in Appendix A. It compares quite well with the strain measurements by the distributed strain sensing (DSS) optical fibre cable in the Zeerijp 3a well over a period of 18 months gas production, see Cannon and Kole (2016) and compaction data derived from core samples from the Zeerijp 3a well, see Hol et al. (2018).

Without having a detailed well log in the Carboniferous, we expect similar variations of the porosity with depth as in the reservoir albeit with a lower value for the mean porosity. The porosity profile of the lower part of the reservoir has been used to generate an artificial profile in the Carboniferous with a shift to a lower mean porosity, see Figure A.4.

The mechanical properties of the other subsurface formations around the fault are listed in Table 2.2. They are derived from the elastodynamic rock properties of the subsurface formations. In particular, they have been calculated from the rock density  $\rho$  [kg/m<sup>3</sup>] and the primary (P) and secondary (S) wave velocities  $V_p$  and  $V_s$  [m/s]. These velocities originate from NAM's seismic velocity model of 2015 and was also used in Wentinck (2017) and Wentinck (2018b)<sup>8</sup>.

We assume, as often done, that the dynamic Young modulus is twice the quasi-static one

<sup>7</sup>According to van Eijs and van der Wal (2017), improvements to the original work of Waal (1986) led to the definition of the so-called isotach (i) formulation of the rate-type compaction model (RTCiM) which was also implemented by NAM.

<sup>8</sup>The NAM model has been provided by Remco Romijn from NAM in the form of Excel and .csv files.

and the dynamic and quasi-static Poisson ratio's are equal.

The relatively stiff anhydrite layer on top of the reservoir has been modelled explicitly. Since it is unlikely that the rupture can propagate into the salt above the reservoir a detailed mechanical model for the overburden is not needed. Hence, the lower and upper Zechstein and the relative thin floater are combined to form one formation with the properties of the lower Zechstein. The properties of the overburden formation above the Zechstein are hardly relevant for this study but have values for the Trias formation above the Zechstein.

The geomechanical properties of the Carboniferous underburden vary with depth. The dynamic Young modulus is calculated from the P and S waves velocities which depend on depth  $z$  [m] according to  $V_p = V_{p0} + k_p \text{abs}(z)$  and  $V_s = V_{s0} + k_s \text{abs}(z)$  where  $V_{p0} = 2572$  m/s,  $k_p = 0.541 \text{ s}^{-1}$ ,  $V_{s0} = 837$  m/s and  $k_s = 0.5 \text{ s}^{-1}$ , using conventional geomechanical relations<sup>9</sup>.

Table 2.2 : Quasi-static mechanical properties of the subsurface formations around the fault. The Young modulus and Poisson ratio in the Carboniferous underburden vary with depth. Values for 3.0, 3.2 and 3.4 km depth follow from expressions for the P and S wave velocities, with a correction for a difference between the static and dynamic Young moduli of a factor 2.

formation	depth	density	Young modulus	Poisson ratio
	km	g/cm <sup>3</sup>	GPa	-
.....	.....	.....	.....	.....
overburden		2.02	24.4	0.29
Zechstein		2.15	23.7	0.29
anhydrite		2.84	45.3	0.26
Rotliegend reservoir (typical values)		2.43	15.0	0.20
Carboniferous underburden	3.0	2.65	18.4	0.27
	3.2	2.65	19.8	0.26
	3.4	2.65	21.3	0.25

<sup>9</sup>These are  $E_{dyn} = \rho V_s^2 (3V_p^2 - 4V_s^2) / (V_p^2 - V_s^2)$  and  $\nu_{dyn} = (V_p^2 - 2V_s^2) / (2(V_p^2 - V_s^2))$ .

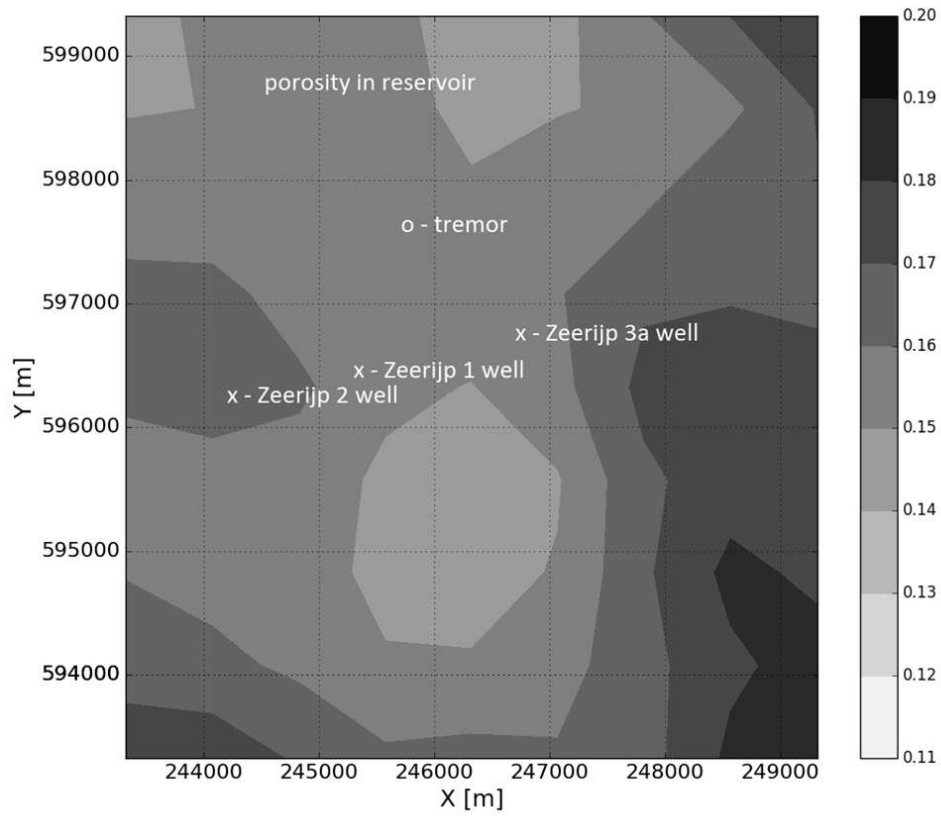


Figure 2.4 : Mean porosity of the reservoir in the region around the Zeerijp epicentre and the locations of the tremor epicentre and the Zeerijp 1, 2 and 3a wells of which well logs have been used for this report. The mean porosity is used in reservoir compaction models and originates from the static geological model from NAM.

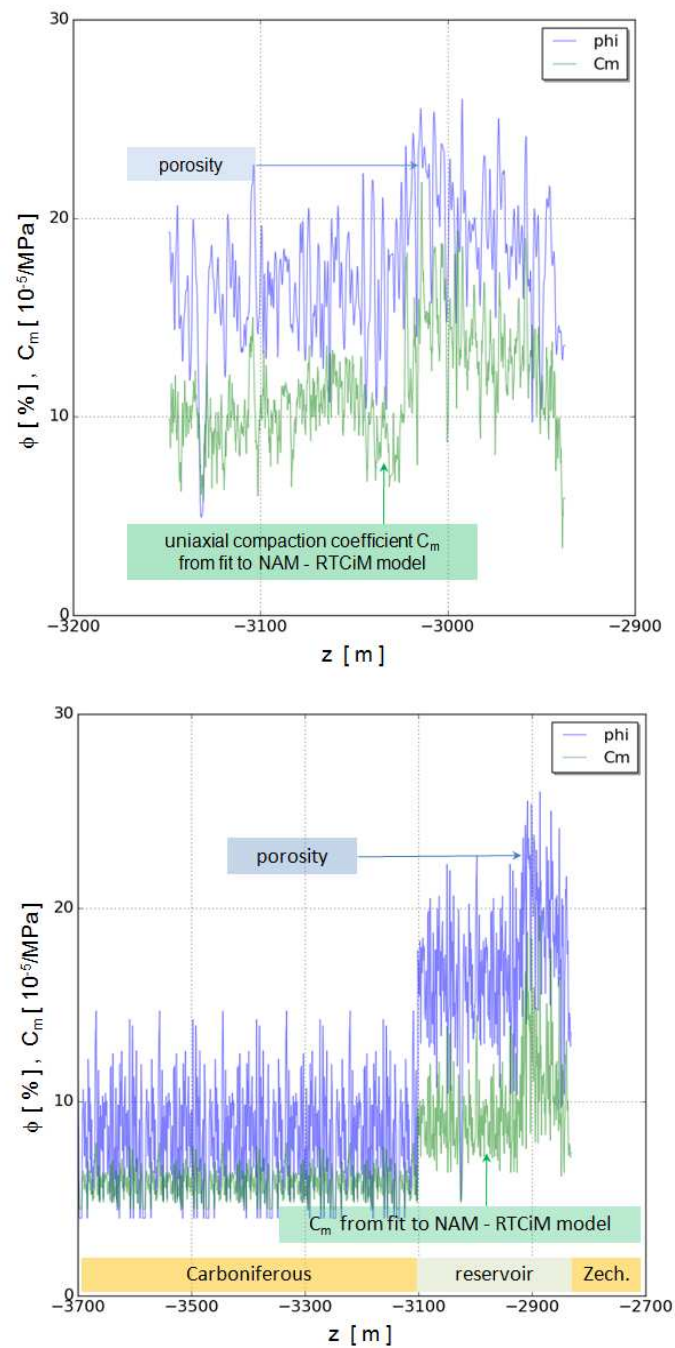


Figure 2.5 : Top figure: profiles of the porosity and uniaxial compaction modulus as a function of depth according to the well log of the Zeerijp 3a well.

Bottom figure: porosity profile used in the simulations with an artificial extension of the lower part of the porosity profile in the reservoir into the Carboniferous. We assume that the average porosity in the Carboniferous is about 8%.

## 2.4 Input for constitutive models for rock failure and seismic slip

There are various constitutive models in the literature for dynamic rupturing and various earthquake experts prefer different models. We have used Ohnaka's strain strengthening/weakening model for which the frictional resistance  $\tau$  [Pa] depends on the slip or relative tangential displacement  $D$  [m] and the normal effective stress on the fault  $\sigma'_n$  [Pa], i.e.,

$$\tau = \mu\sigma'_n \quad \text{where} \quad \mu = \mu_r + (\mu_s - \mu_r)(1 + \alpha \log(1 + \beta D)) \exp(-\eta D). \quad (2.1)$$

$\mu_s$  and  $\mu_r$  [-] are the static and dynamic (or residual) friction coefficients.  $\alpha$  [-] and  $\beta$  [ $\text{m}^{-1}$ ] are two input parameters which define the slip required for maximal frictional resistance or the start of failure.  $\eta \propto 1/D_c$  [ $\text{m}^{-1}$ ] defines the slip required to obtain residual frictional resistance, see Ohnaka (2013), §2.2.  $D_c$  [m] is the so-called critical breakdown slip (or characteristic slip weakening distance or critical breakdown relative displacement), see for more details Appendix B. Both curves have a comparable slip-weakening rate parameter  $W$ , see Appendix B, Eq. (B.4). The values of  $D_c$  are typical for the magnitude of the Zeerijp tremor, see for example Ohnaka (2013), Fig. 5.21<sup>10</sup>.

For all simulations, the fault width is 1 m.  $\mu_s = 0.6$ ,  $\alpha = 30$  and  $\beta = 80 \text{ m}^{-1}$  for both the reservoir and the Carboniferous. For the non-brittle or ductile Zechstein, the static and dynamic friction coefficients are equal.  $\alpha$ ,  $\beta$  and  $\eta$  are supposed to be uniform along the fault plane. The input parameters, which have been varied in the simulations, are given in Table 2.3 .

In the relatively thin fault gouge of the fault zone relatively slow non-elastic micro-mechanical processes may take place due to the imposed shear stress from gas production, in particular at locations where the shear stress is high during compaction. One possibility to incorporate this effect in the constitutive model is by adding differential equations for elastic strain relaxation on the two surface on both sides of the fault zone. The 'creep' model used has one time constant  $t_{creep}$  [s], see Appendix B, §B.4<sup>11</sup>.

In this work, we have added little creep to trigger the rupture at the required reservoir pressure while keeping the other input parameters of the constitutive model constant.

---

<sup>10</sup>According to this reference,  $M_0 \propto D_c^3$  while the breakdown stress drop  $\Delta\tau$  is independent on the seismic moment.

<sup>11</sup>For example, for  $t_{creep} = 10^{10}$  s half of the deformation in the fault zone will be lost for strain-strengthening/weakening and herewith for fault instability in a period of about 300 years.

Table 2.3 : Input parameters for Ohnaka's constitutive model for fault failure and other parameters for simulations A and B, see also §3.2. To compare these parameters with those for a linear strain weakening model, a more or less equivalent critical breakdown slip  $D_{c,equiv}$  is calculated from  $D_{c,equiv} = 5/\eta$ , see also Figure 2.6 . The parameters for simulation A2 without strain hardening are not included in this table but given in Appendix D.

Simulations		A1/3/4	B1/2/3
Property	unit	value	value
.....	.....	.....	.....
$\alpha$	-	30	
$\beta$	$m^{-1}$	80	
reservoir			
$\eta$	$m^{-1}$	770	666/685
$D_{c,equiv}$	mm	6.5	7.5/7.3
$\mu_r$	-	0.2/0.25	0.2/0.3
Carboniferous			
$\eta$	$m^{-1}$	770	666/685
$D_{c,equiv}$	mm	6.5	7.5/7.3
$\mu_r$ Carboniferous	-	0.2/0.25/0.4	0.2/0.3/0.4
a-seismic relaxation in fault zone			
$t_{creep}$	year	320	160
other parameters			
fault dip $\delta$	degrees	80	75

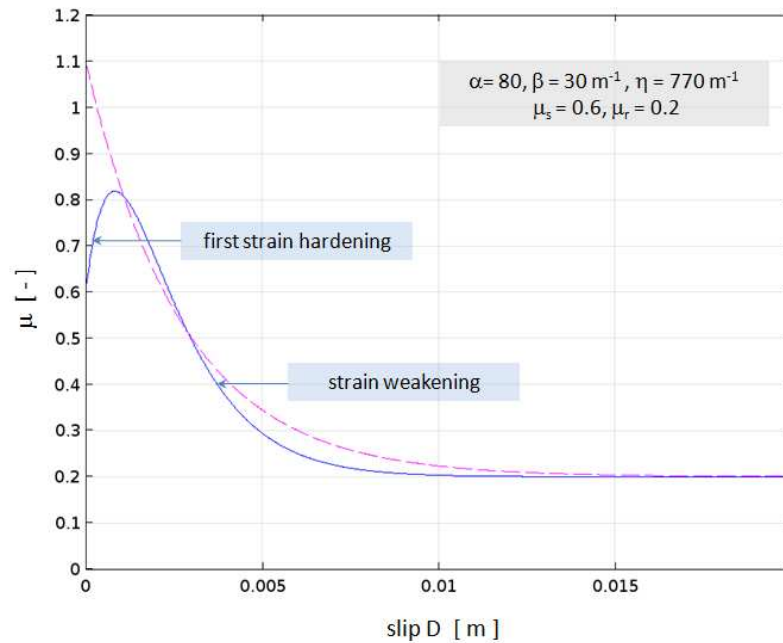


Figure 2.6 : Constitutive model for the friction coefficient  $\mu$  as a function of slip  $D$  for typical parameters according to Ohnaka's strain strengthening/weakening model, see Ohnaka (2013), §2.2. The blue line is according to the input parameters in Table 2.3 . In this case, considerable strain strengthening within a slip distance of about 1 mm is followed by strain weakening within a slip distance of 5 - 10 mm. The dashed magenta line follows from Ohnaka's constitutive model used in Appendix D for simulation A2 without strain strengthening.

## 2.5 Input parameters for pressure diffusion in the Carboniferous

We suppose that pressure diffusion into the Carboniferous underburden below the reservoir starts at the bottom of the reservoir and is uniform in lateral direction. The reservoir pressure at the horizon between the Carboniferous and reservoir decreases over time as in the main body of the reservoir.

The permeability of the Carboniferous is much lower than the permeability of the reservoir but poorly known. However, it is not unreasonable to expect that during gas production over a period of about 60 years and a reservoir pressure drop of about 50 years, pressure changes in the reservoir diffuse over tenths of meters into the Carboniferous for an expected permeability in the microDarcy range. This can be estimated from the diffusion constant  $D_{p,cb}$  [m<sup>2</sup>/s] for pressure diffusion into a porous rock. Take the following one-dimensional pressure diffusion equation over depth  $z$ [m],

$$\frac{\partial p}{\partial t} = D_{p,cb} \frac{\partial^2 p}{\partial z^2} \quad \text{where} \quad D_{p,cb} = \frac{k_{cb}}{\phi_{cb} \mu_f \kappa_f}. \quad (2.1)$$

$k_{cb}$  [m<sup>2</sup>] and  $\phi_{cb}$  [-] are the permeability and the porosity in the upper part of the Carboniferous,  $\mu_f$  [Pa.s] is the viscosity of the fluid in the Carboniferous and  $\kappa_f$  [1/Pa] is the compressibility of the fluid which fills the pores in the Carboniferous rock.

Using  $k_{cb} = 0.3 \mu\text{D}$ ,  $\phi_{cb} = 0.08$  and for brine with some gas in the Carboniferous<sup>12</sup>,  $\mu_f = 0.5 \text{ mPa.s}$  and  $\kappa_f = 2.10^{-8} \text{ Pa}^{-1}$ , we have  $D_{p,cb} = 3 \cdot 10^{-7} \text{ m}^2/\text{s}$ . This would mean that in a period of  $t_{pen} = 50$  years, a pressure change at the top of the Carboniferous penetrates over a characteristic length  $L_{pen,cb} = \sqrt{D_{p,cb} t_{pen}} \sim 25 \text{ m}$ .

---

<sup>12</sup>For brine,  $\mu_f \sim 5.10^{-4} \text{ Pa.s}$  and  $\kappa_f \sim 4.10^{-10} \text{ Pa}^{-1}$ . For natural gas at a pressure and temperature of 30 MPa and 80°C,  $\mu_f \sim 2.10^{-5} \text{ Pa.s}$  and  $\kappa_f \sim 2.5 \cdot 10^{-8} \text{ Pa}^{-1}$ . For a Carboniferous with only brine or only gas, a pressure change would penetrate farther into the Carboniferous.

# Chapter 3

## Results

### 3.1 Set-up of simulations

The two dimensional dynamic rupture simulations have been performed using COMSOL<sup>TM</sup> with the standard structural mechanics module for elasto-dynamic media. The simulations are under the condition of plane strain and in time-dependent mode. The reservoir is modelled as a non-uniform thermo-elastic medium using the analogy between poro-elasticity and thermo-elasticity. The gas pressure is replaced by an equivalent temperature and the poro-elastic constants by equivalent thermo-elastic constants. The other subsurface formations are modelled as elastic media, see Figure 3.1 for the geometry of the two-dimensional subsurface model, in agreement with the dimensions given in Table 2.1 .

The field stress is imposed on the fault by standard geomechanical techniques using the superposition principle that can be applied for elastic media. The stress development on the fault plane and the response of the fault on the compaction stress, including some creep, as governed by the constitutive equations is treated as a boundary value problem on the surfaces of the fault zone, see Appendix B.

The loading of the fault by field and compaction stresses is in time-dependent mode. The structural transitional behaviour of the rock is simulated as quasi-steady. The onset of fault instability during loading is detected by a relatively fast drop in the friction coefficient on the fault and a fast reduction of the time steps required to meet convergence criteria<sup>1</sup>. After the onset of fault instability, the simulation is continued in full dynamic mode. During the rupture process, the structural transitional behaviour of the rock includes the inertial terms.

The mesh used in the simulations is refined to cells of about 1 m on the fault plane

---

<sup>1</sup>This method is less rigorous than the method used by van den Bogert (2018b) to detect fault instability. In practice, varying the values of these rate type criteria for fault instability, does not lead to significant different results.

according to criteria from the literature<sup>2</sup>. Using a two times less refined mesh give similar results. The time-dependent solver used under default settings is called ‘Generalized Alpha’. The time step during fault rupture is maximised to 1 ms.

The critical breakdown slip  $D_c$ , and within reasonable bounds the time constant  $t_{creep}$ , have been varied to have a rupture at the required reservoir pressure of about 9 MPa. The residual friction coefficient  $\mu_r$  has been varied to obtain sufficient slip and breakdown stress drop in accordance with the observed ground displacements and moment magnitude.

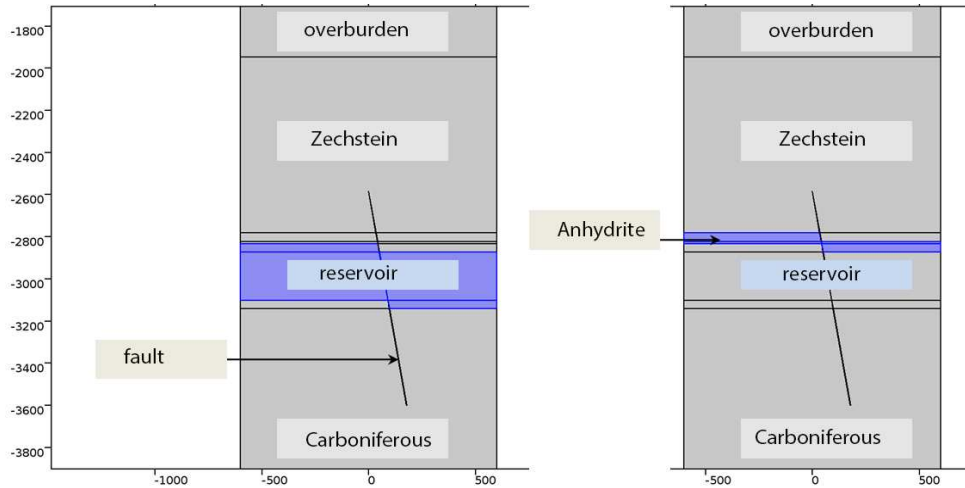


Figure 3.1 : Geometry of the simulations. The left figure shows the domain of the reservoir in blue. The right figure shows the domain of the relatively thin anhydrite formation on top of the reservoir in blue. On the left side of the fault plane the well log profile is 20 m shifted upwards and on the right side of the fault plane, the well log profile is 20 m shifted downwards.

<sup>2</sup>For accurate results, the grid spacing should be about 2 - 5 times smaller than the length of the cohesive zone of the rupture front where slip weakening on the fault plane takes place  $\Gamma_c$ , see for example Day et al. (2005), Fig. 4.

A simple estimate for  $\Gamma_c$  for linear strain weakening is given by Eq. 30a in this reference, i.e.,  $\Gamma_c \sim \mu D_c / \Delta\tau$ , which is comparable to the dimension of the nucleation zone, see Appendix B.  $\Delta\tau$  [Pa] is the part of the shear stress on the fault plane which is released by the rupture, or the breakdown stress drop,  $\mu$  [Pa] is the shear modulus of the rock and  $D_c$  [m] is the so-called critical breakdown slip.

For  $\mu = 6$  GPa,  $\Delta\tau = 3$  MPa, we have  $\Gamma_c \sim 2 \cdot 10^3 D_c$ . For a minimum value of  $D_c = 5$  mm,  $\Gamma_c \sim 10$  m and a grid spacing of about 1 m on the fault plane is sufficient.

## 3.2 Results

Two simulations A and B have been carried out, varying the stress condition on the fault by varying the fault dip and, see Table 2.3 . For simulation A, the fault dip is  $\delta = 80^\circ$  resulting in a small shear stress on the fault before compaction, i.e.,  $\tau_{field} \sim 3$  MPa. The residual friction coefficient  $\mu_r$  is varied for the reservoir and the Carboniferous to investigate which values are needed to obtain sufficient breakdown stress drop and which values prevent penetration of the rupture into the Carboniferous.

For simulation B, the fault dip is  $\delta = 75^\circ$  leading to a higher shear stress on the fault before compaction, i.e.,  $\tau_{field} \sim 5$  MPa. Again,  $\mu_r$  is varied for the reservoir and Carboniferous for the same reasons.

We show below the main results of simulation A. Other results of simulation A and results of simulation B are shown in Appendix D. Figure 3.2 shows the stresses on the fault and the pressure profile before compaction and before rupture. Figure 3.3 shows the slip just before and during rupture. Figure 3.4 shows the slip during rupture for two other combinations of residual friction coefficients. Figure 3.5 shows the breakdown stress drop for the three cases.

Before rupture, the shear stress on the fault increases from about 3 MPa to about 5 - 12 MPa due to compaction following gas production. The shear stress spikes where the reservoir-anhydrite horizon on the right side of the fault is juxtaposed to the reservoir rock on the left side and in the centre of the reservoir because the non-uniform reservoir rock is 40 m higher on the left side than on the right side of the fault. A peak in the shear stress at the Carboniferous-reservoir horizon is less pronounced because of pressure diffusion into the Carboniferous.

Low residual friction coefficients are required to obtain sufficient breakdown stress drop and sufficient slip. Increasing  $\mu_r$  from 0.2 to 0.25 has already a profound effect on the slip distance. Slip and breakdown stress drop go hand in hand, according to Figures 3.3 , 3.4 and 3.5 .

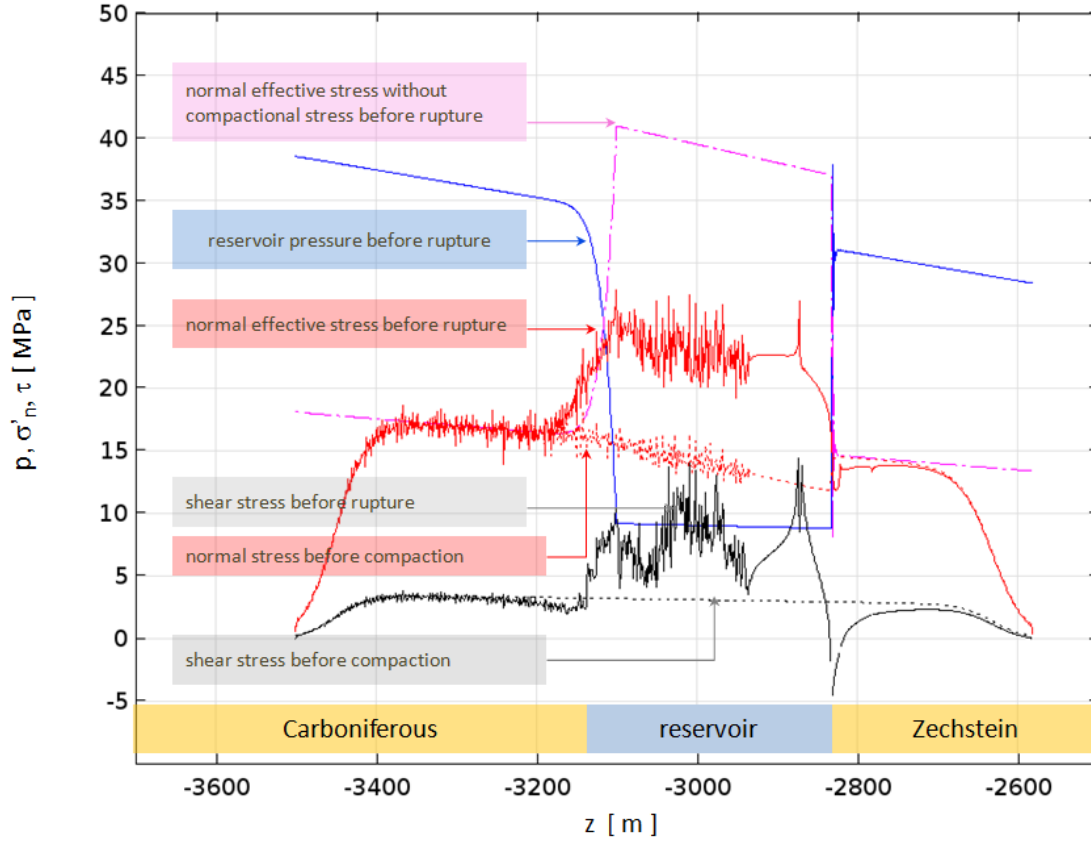


Figure 3.2 : Simulation A1: pressure in the reservoir and in the upper part of the Carboniferous and the stress on the fault before compaction and before rupture as a function of depth. The fault dip angle  $\delta = 80^\circ$ . The black dotted and solid lines show the shear stresses before compaction and just before rupture, respectively. The red dotted and solid lines show the normal effective stresses before compaction and just before rupture, respectively.

The blue line shows that the pressure drop in the reservoir has penetrated into the Carboniferous over a period of almost 60 years gas production. Herewith, the normal effective stress (red line) in the upper part of this formation also increases. The effect of differential compaction in a non-uniform reservoir on the normal and shear stresses is clearly seen by the spikes in the solid black and red lines.

The dashed-dotted magenta line shows the normal effective stress  $\sigma'_n$  before rupture if there would have been a pressure drop in the reservoir but no compaction. Due to compaction,  $\sigma'_n$  on this near vertical fault drops about 15 MPa, in accordance with a poro-elastic reduction in the horizontal effective stress of about  $\Delta\sigma'_h = \gamma_h \Delta p$  where  $\gamma_h = \alpha(1 - 2\nu)/(1 - \nu)$ . For  $\delta p \sim 26$  MPa,  $\nu \sim 0.2$  and  $\alpha \sim 0.8$ , we have  $\gamma_h \sim 0.6$  and  $\Delta\sigma'_h \sim 16$  MPa.

The stresses drop to zero at the upper and lower ends of the fault. This stress reduction is artificial to speed up calculations. It has no effect on the compaction and rupture processes in the reservoir and in the upper part of the Carboniferous.

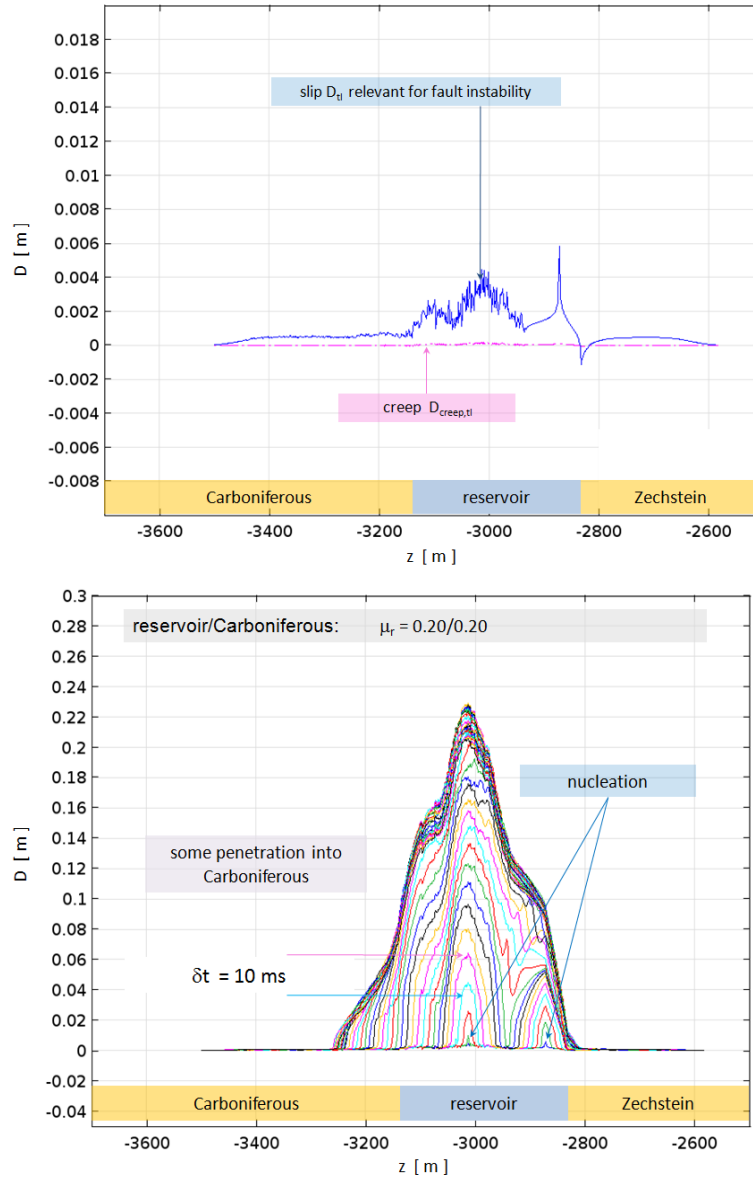


Figure 3.3 : Simulation A1: slip or relative displacement  $D_t$  along the fault versus depth just before (top figure) and during rupture (bottom figure).

Top figure: just before rupture, local slip along the fault exceeds the equivalent critical breakdown slip  $D_{c,equiv} = 0.008$  m.  $\mu_r = 0.2$  in the reservoir and in the Carboniferous. The displacement due to creep along the fault (pink line) is less than 5% of the total displacement.

Bottom figure: slip during rupture. The contour lines show snapshots for time steps every 10 ms. From the distances between these lines close to the horizontal axis and the time intervals, a maximum rupture velocity in downwards direction in the lower stressed part of the fault can be derived of  $\sim 1$  km/s.

The nucleation starts in this simulation at two locations along the fault plane. The part of the fault plane between these two nucleation patches slips faster than the rest of the fault. This can be concluded from the distance between the contour lines. A faster slip contributes to larger ground motion accelerations.

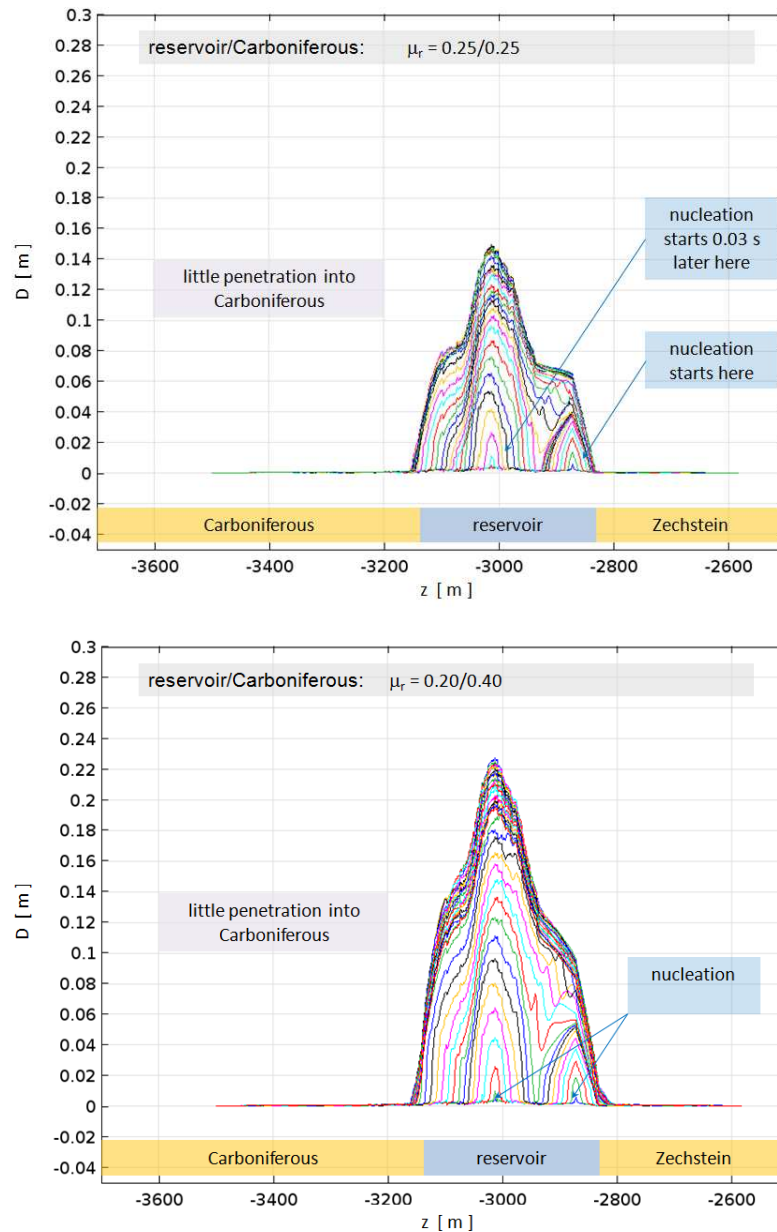


Figure 3.4 : Simulations A3 and A4: slip or relative displacement along the fault plane  $D$  during rupture for two other combinations of residual friction coefficients in the reservoir and in the Carboniferous.

Top figure: simulation A3,  $\mu_r = 0.25$  in the reservoir and in the Carboniferous. Bottom figure: simulation A4,  $\mu_r = 0.2$  in the reservoir and  $\mu_r = 0.4$  in the Carboniferous.

The slip reduces about 40% when  $\mu_r$  is increased from 0.2 to 0.25, see Figure 3.3 for the case  $\mu_r = 0.2$ . When  $\mu_r$  is increased from 0.2 to 0.4 in the Carboniferous, the rupture is arrested at the bottom of the reservoir while the slip in the reservoir is similar as in Figure 3.3 .

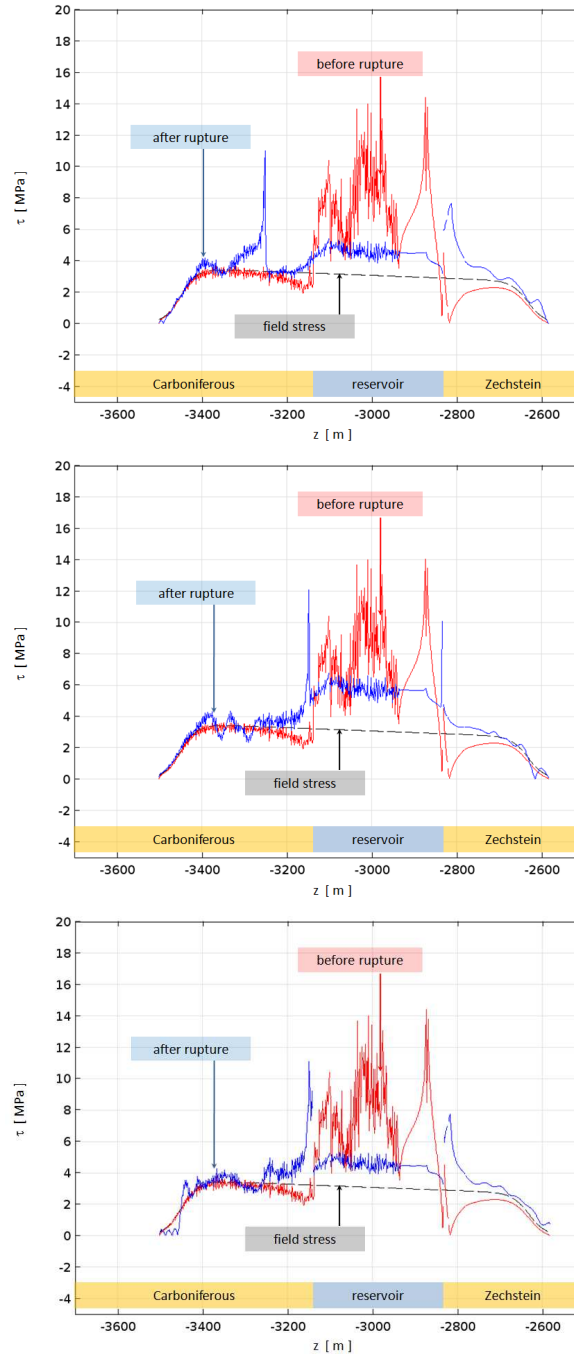


Figure 3.5 : Simulations A1, A3 and A4: breakdown stress drop over the fault plane. For reference, the black dashed lines show the shear stress due to the field stress.

Top figure: simulation A1,  $\mu_r = 0.2$  in the reservoir and in the Carboniferous. Centre figure: simulation A3,  $\mu_r = 0.25$  in the reservoir and in the Carboniferous. Bottom figure: simulation A4,  $\mu_r = 0.2$  in the reservoir and  $\mu_r = 0.4$  in the Carboniferous.

Comparing the top and centre figures, the breakdown stress drop considerably reduces with the slip or relative displacement along the fault plane  $D$ . Comparing the top and bottom figures, the average breakdown stress drop in the Carboniferous is less for  $\mu_r = 0.4$  in this formation.

# Chapter 4

## Discussion

The simulations show that compaction in a non-uniform reservoir can lead to a considerable shear stress, like on the mFS7-Fault-54 fault with a large dip angle and relatively little throw. For this fault, shear stresses are high in the centre of the reservoir. The simulations show also that stress changes due to pressure depletion in the upper part of the Carboniferous are important. We recommend to include these additional features in future dynamic rupture simulations.

So far, we have disregarded the more complex fault structure of the mFS7-Fault-54 fault with a nearby reverse fault near the hypocentre. It must be sorted out whether the nearby reverse fault would have a significant effect on the stress on the fault plane which ruptured.

Despite remaining uncertainties about the constitutive parameters determining fault failure and the stress condition on the fault at the tremor hypocentre, the analysis of the Zeerijp tremor indicates that there must be a considerable drop in the frictional resistance during rupture. A considerable breakdown stress drop is needed to generate the amount of seismic energy observed from the ground motions in a relatively short time from this nearly vertical fault with relatively little throw and high dip angle.

This can also be concluded from similar work by van den Bogert (2018a), using a linear strain weakening model. If there would be no considerable breakdown stress drop, additional forces are needed from tectonic origin or from additional stresses following from the more complex fault geometry around the tremor hypocentre.

On the other hand, the static and/or the residual friction coefficient of the Carboniferous rock should be considerably higher than the values of the Rotliegend sandstone to prevent significant penetration of ruptures into the Carboniferous underburden. This holds especially for faults with a higher shear stress along the fault plane, such as those with a lower dip angle, or loaded by additional shear forces along fault strike.

More or less creep in the fault zone does not change these results. To reduce the present uncertainties about the input parameters for the constitutive equations for fault failure, we recommend friction measurements under realistic subsurface conditions at seismic slip velocities of 0.1 - 2 m/s under fast accelerations. Such experiments should complement

friction experiments at low slip velocities, i.e., below 0.01 m/s which are currently done to study the onset of fault instability<sup>1</sup>.

According to the simulations, the maximum rupture velocity along fault dip is  $V_{r,max} \sim 1$  km/s, which is considerably less than a rupture velocity of 80 - 90% of the shear wave velocity, frequently used. The main reason is that outside the nucleation patches, the stress condition on the fault is quite far from critical. In a simulation where strain hardening is absent, we have for a short time  $V_{r,max} \sim 2$  km/s. The higher rupture velocity follows from another stress redistribution over the fault during rupturing because of a different nucleation of critically loaded fault patches.

The triggering of nucleation patches along the fault plane depends on subtle factors, such as non-uniform compaction and the development of fault resistance for small slip. Further, it could well be that rupture velocities along fault strike are higher where highly stressed zones are well connected. So far, we have not derived with confidence the rupture velocity along dip from observations to constrain model parameters further.

---

<sup>1</sup>High velocity friction experiments have been done by Giulio Di Toro (Univ. of Padova, Italy) for other rocks, like gabbro or containing clay, see for example Ferri et al. (2011). They should be repeated for the Rotliegend sandstone and for the Carboniferous underburden and in particular for representative stresses and displacements. Such experiments could be done by the group of Chris Spiers from the University of Utrecht and by the group of Giulio Di Toro.

# Chapter 5

## Acknowledgements

I thank Peter van den Bogert (SGS-I), Roger Yuan (SGS-I) and Loes Buijze (Univ. of Utrecht, Netherlands) for discussions on dynamic rupture models and Sander Hol (SGS-I), Arjen Niemeijer (Univ. of Utrecht, Netherlands), Chris Spiers (Univ. of Utrecht, Netherlands) and Giulio Di Toro (Univ. of Padova, Italy) for discussions on the constitutive relations for dynamic rupture models. I thank Onno van der Wal (NAM), Pepijn Kole (NAM), Math Cannon (SGS-I), Rob van Eijs (NAM), Leendert Geurtsen (NAM) and Quint de Zeeuw (NAM) for providing me the Zeerijp well logs, compaction data and reservoir data of the Groningen field.

I thank Remco Romijn (NAM) and Clemens Visser (NAM) for providing me the field data and the subsurface velocity model, Marloes Kortekaas (EBN) and Alan Wood (SGS-I) for providing me fault data from ant-tracking around the Zeerijp tremor epicentre, Bernard Dost (KNMI) and Ewoud van Dedem (SGS-I) for providing a plausible fault orientation and slip direction from moment tensor inversion methods. I thank all and also Steve Oates (SGS-I) for many comments and suggestions.

# Bibliography

- Aki, K., and Richards, P. G., “Quantitative Seismology”, University Science Books, 2009.
- Buijze, L., Orlic, B., and Wassing, B. B. T., “Modeling of Dynamic Fault Rupture in a Depleting Gas Field”, Technical Report TNO 2015 R10844, TNO, the Netherlands, 2015.
- Cannon, M., and Kole, P., “The First Year of Distributed Strain Sensing (DSS) Monitoring in the Groningen Gas Field”, Technical Report SR.17.00934, Shell Global Solutions International B.V., 2016.
- Chen, J., and Spiers, J. C., “Rate and State Frictional and Healing Behavior of Carbonate Fault Gouge explained using Microphysical Model”, *Journ. of Geophysical Research: Solid Earth*, 121, 8642–8665, 2017.
- Day, S. M., Dalguer, L. A., and Lapusta, N., “Comparison of Finite Difference and Boundary Integral Solutions to Three-dimensional Spontaneous Rupture”, *Journ. of Geophysical Research*, 110, 1–23, 2005.
- Dieterich, J. H., “Modeling of rock friction: 1. Experimental results and constitutive equations”, *Journ. of Geophysical Research*, 84, 2161–2168, 1979.
- Dost, B., and Kraaijpoel, D., “The August 16, 2012 Earthquake near Huizinge (Groningen)”, Technical Report KNMI report TR 16/1/2013, Koninklijke Nederlands Meteorologisch Instituut, the Netherlands, 2013.
- Dost, B., Edwards, B., and Bommer, J. J., “The Relationship between  $M$  and  $M_L$ : A Review and Application to Induced Seismicity in the Groningen Gas Field, The Netherlands”, *Seism. Res. Letters*, 89, 1062–1074, 2018.
- Ferri, F., Toro, G. D., Hirose, T., Han, R., Noda, H., Shimamoto, T., Quaresimin, M., and de Rossi, N., “Low- to High-velocity Frictional Properties of the Clay-rich Gouges from the Slipping zone of the 1963 Vaiont slide, northern Italy”, *Journ. of Geophysical Research*, 116, 1–17, 2011.
- Fjaer, E., Holt, R. M., Horsrud, P., Raaen, A. M., and Risnes, R., “Petroleum related Rock Mechanics in Developments in Petroleum Science, 2nd edition 53”, Elsevier, Amsterdam, 2008.

- Galis, M., Pelties, C., Kristek, J., Moczo, P., Ampuero, J.-P., and Mai, P. M., “On the Initiation of Sustained Slip-weakening Ruptures by Localized Stresses”, *Geophys. J. Int.*, 200, 888–907, 2015.
- Hol, S., van der Linden, A., Bierman, S., Marcelis, F., and Makurat, A., “Rock Physical Controls on Production-induced Compaction in the Groningen Field”, *Physical Reports*, [www.nature.com](http://www.nature.com), 8:7156, 1–13, 2018.
- Leonard, M., “Earthquake Fault Scaling: Self-Consistent Relating of Rupture Length, Width, Average Displacement, and Moment Release”, *Bull. of the Seism. Soc. of America*, 100, 1971–1988, 2010.
- Ohnaka, M., “The Physics of Rock Failure and Earthquakes”, Cambridge University Press, 2013.
- Sanz, P. F., Lele, S. P., Searles, K. H., Hsu, S. Y., and Garzon, J. L., “Geomechanical Analysis to Evaluate Groningen Production Scenarios”, Technical Report 20150209, ExxonMobil Upstream Research Company Houston, TX, 2015.
- Scholz, C. H., “The Mechanics of Earthquakes and Faulting, 2<sup>nd</sup> edition”, Cambridge University Press, 2002.
- Stein, S., and Wysession, M., “An Introduction to Seismology, Earthquakes, and Earth Structure”, Blackwell Publishing, 2003.
- Udias, A., Madariaga, R., and Buforn, E., “Source Mechanisms of Earthquakes - Theory and Practice”, Cambridge University Press, 2014.
- Uenishi, K., and Rice, J. R., “Universal Nucleation Length for Slip-Weakening Rupture Instability under Non-uniform Fault Loading”, *Journ. of Geophysical Research*, 108, 2042–2056, 2003.
- van den Bogert, P. A. J., “Seismic Rupture related to the Zeerijp Tremor”, Technical Report SR.18.XXXXX, Shell Global Solutions International B.V., 2018.
- , “Understanding Fault Stability and Seismic Rupture in Depleting Reservoirs with Offset 2-D Dynamic Rupture Simulation”, Technical Report SR.18.XXXXX, Shell Global Solutions International B.V., 2018.
- van Eijs, R., and Valencia, K., “Minimum horizontal Stress information in the Groningen Field (Rotliegendes Formation)”, Technical Report EP-2013-011200514, Shell International Exploration and Production, 2013.
- van Eijs, R. M. H. E., and van der Wal, O., “Field-wide Reservoir Compressibility Estimation through Inversion of Subsidence Data above the Groningen Gas Field”, *Netherlands Journal of Geosciences Geologie en Mijnbouw*, 96, 117–129, 2017.

- Waal, J. A. D., “On the Rate Type Compaction Behaviour of Sandstone Reservoir Rock” ,, Technical Report PhD Thesis, Technical University Delft, The Netherlands, 1986.
- Wentinck, H. M., “Kinematic Modelling of Large Tremors in the Groningen Field using Extended Seismic Sources - First Results related to the Huizinge 2012 Tremor” ,, Technical Report report for NAM, Shell Global Solutions International B.V., 2017.
- Wentinck, H. M., “Kinematic Modelling of Large Tremors in the Groningen Field using Extended Seismic Sources - First Results related to the Zeerijp tremor  $M_L$  3.4” ,, Technical Report report for NAM, Shell Global Solutions International B.V., 2018.
- , “Kinematic Modelling of Large Tremors in the Groningen Field using Extended Seismic Sources - Second Results related to the Huizinge 2012 Tremor” ,, Technical Report report for NAM, Shell Global Solutions International B.V., 2018.



# Appendix A

## Correlation between porosity and uniaxial compaction coefficient

Figure A.1 shows the porosity profiles in the Zeerijp 1, 2 and 3a wells. They are quite comparable and show that the reservoir is non-uniform. In the upper 80 m of the reservoir the porosity is above 20%, in the lower part it is about 17%.

The following relations are used between the mean porosity  $\phi$  [-], uniaxial compaction coefficient  $C_m$  [1/Pa] and other mechanical rock properties. According to poro-elastic theory, see for example Fjaer et al. (2008), Eq. 12.10,

$$C_m = \frac{1}{E} \frac{(1 + \nu)(1 - 2\nu)}{1 - \nu}. \quad (\text{A.1})$$

$E$  [Pa] is the Young modulus and  $\nu$  [-] is the Poisson ratio. The uniaxial strain in a uniform reservoir in the z-direction along depth,  $\epsilon_z = \Delta h/h$  [m/m] due to a pressure drop  $\Delta p$  [Pa] follows from

$$\epsilon_z = \frac{\Delta h}{h} = C_m \alpha \Delta p = C'_m \Delta p. \quad (\text{A.2})$$

$h$  [m] is the reservoir thickness and  $\Delta h$  [m] is the change in the reservoir thickness due to compaction.  $\alpha = 1 - K/K_s$  is the Biot constant where  $K = E/(3(1 - 2\nu))$  [Pa] is the bulk modulus of the rock and  $K_s$  [Pa] is the bulk modulus of the grains of the rock.  $C'_m$  [1/Pa] is the so-called apparent uniaxial compression coefficient, often used when statements about the value of the Biot coefficient are not made.

For a geomechanical analysis of the Groningen field using Abacus<sup>TM</sup>, Sanz et al. (2015), Fig. 4.7 show fits for the Young modulus  $E$  [Pa] and the Poisson ratio  $\nu$  [-] as a function of porosity  $\phi$  [-] to a set of data of Rotliegend sandstone cores. These fits, used by ExxonMobil, can be approximated by the following expressions

$$E = (250\phi^2 - 175\phi + 34) \times 10^9, \quad (\text{A.3})$$

and

$$\nu = 0.106 + 0.315\phi. \quad (\text{A.4})$$

The blue curve in Figure A.4 follows from inserting these expressions in Eq. (A.1).

To calculate reservoir compaction from the subsidence data over time using a statistical inversion method, van Eijs and van der Wal (2017) uses the following least-squared regression function for the apparent compaction coefficient  $C'_m$  based on core data

$$C'_{m,L2} = (267.3\phi^3 - 68.72\phi^2 + 9.85\phi + 0.21)10^{-10}. \quad (\text{A.5})$$

To start the statistical inversion over many small sub-domains in the Groningen field, the so-called 'prior' is  $C'_{m,prior} \sim 0.37C'_{m,L2}$ , according to the green line in Figure 2 in this reference. Using the so-called RTCiM compaction model<sup>1</sup>, Figure A.2 shows a cloud of green dots showing the 'posterior' relation between  $C'_m$  and  $\phi$  for all sub-domains.

A reasonable fit through this cloud of green dots is  $C'_{m,posterior} = 1.7 \times C'_{m,prior}$ . Herewith,  $C'_{m,posterior} = 0.64 \times C'_{m,L2}$  where  $C'_{m,L2}$  is given by Eq. (A.5).

To use for the simulations  $C_m$  and a consistent value for the Young modulus instead of  $C'_m$ , a value for the bulk modulus of the grains  $K_s$  is required. From  $C_m = C'_m/\alpha$  and  $C_m = (1 + \nu)/(1 - \nu)/(3K)$ ,

$$K = \frac{1}{1/K_s + 3C'_m(1 - \nu)/(1 + \nu)}. \quad (\text{A.6})$$

Using  $E = 3(1 - 2\nu)K$ , the Young modulus is given. Since  $1/K_s$  is usually small compared to the term  $3C'_m(1 - \nu)/(1 + \nu)$ , the precise value of  $K_s$  is not so important. We use  $K_s = 40$  GPa and  $\nu = 0.25$  in the simulations.

The Poisson ratio used follows from the Zeerijp 3a well log data. From the P and S wave velocities, the dynamic Poisson ratio can be determined and plotted against the porosity. Assuming that the dynamic Poisson ratio is equal to the static one, linear fit to this data is

$$\nu = 0.16 + 0.42\phi. \quad (\text{A.7})$$

Figures A.3 and A.4 show the correlations for  $C_m$  and  $\nu$  used.

From the distributed strain sensing (DSS) optical fibre cable in the Zeerijp 3a well from Cannon and Kole (2016), the apparent uniaxial compaction coefficient  $C'_m$  and  $C_m = C'_m/\alpha$  can be calculated, assuming that the reservoir pressure over the period of 18 months reduces with a rate of 0.3 MPa/year, i.e., about 0.45 MPa.

The black dots in Figure A.4 originate from cores from the Zeerijp 3a well from Hol et al. (2018). Using again  $K_s = 40$  GPa and  $\nu = 0.25$ , we calculated  $C_m$  values from the apparent uniaxial compaction coefficients provided.

---

<sup>1</sup>According to van Eijs and van der Wal (2017), improvements to the original work of Waal (1986) led to the definition of the so-called isotach (i) formulation of the rate-type compaction model (RTCiM) which was also implemented by NAM.

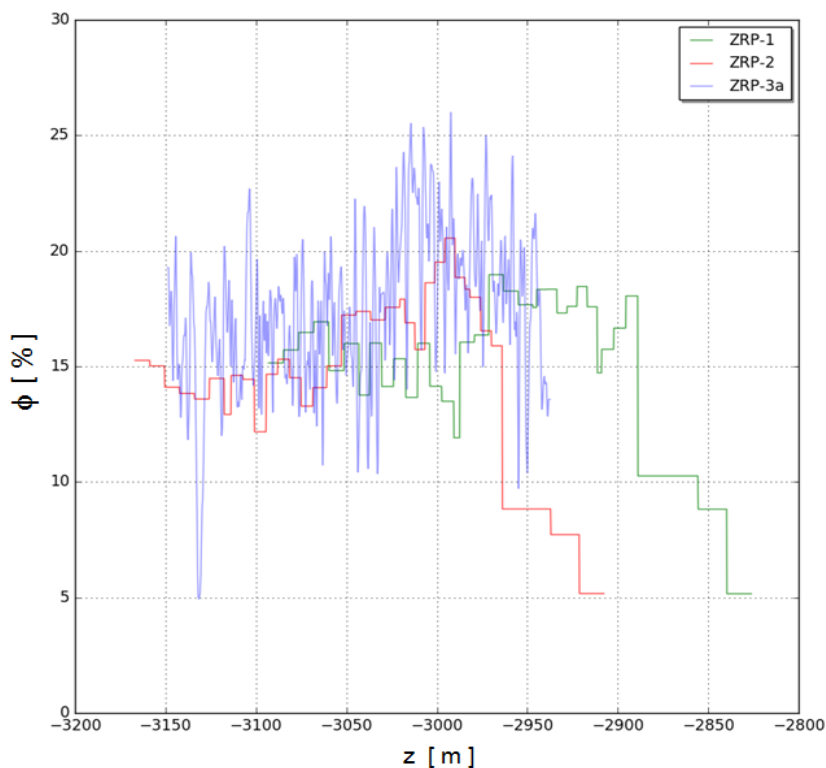


Figure A.1 : Porosity profiles as a function of true vertical depth in the Zeerijp 1, 2 and 3a wells. The profiles of the Zeerijp 1 and 2 wells are similar as the one of the Zeerijp 3a well but less detailed and shifted with respect to the profile of the Zeerijp 3a well over depth because of reservoir depth. Two profiles show a relatively high porosity in the upper part of the reservoir.

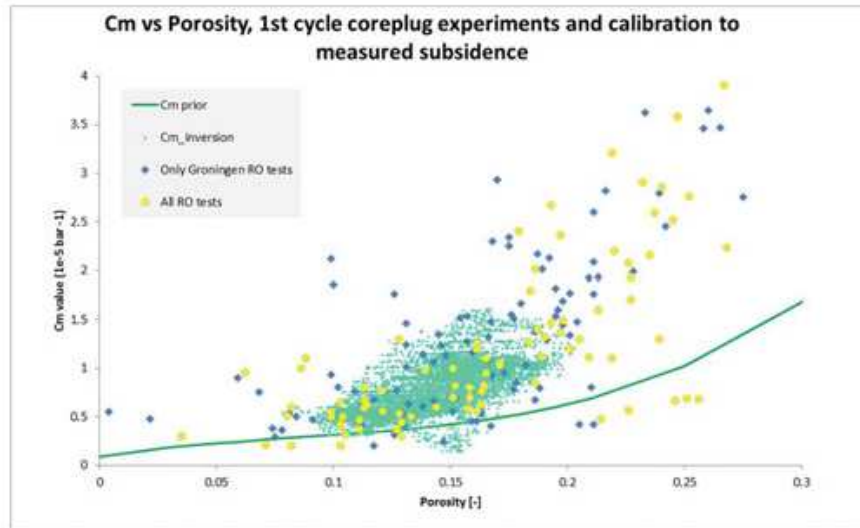


Figure A.2 : The apparent uniaxial compaction coefficient  $C'_m$  versus the mean porosity  $\phi$  according to the RTCiM compaction model, see van Eijs and van der Wal (2017), Figure 7. RO stands for the Rotliegend reservoir rock. The rock samples have been taken from the Slochteren sandstone formation (ROSL).

The green solid line shows the prior correlation between  $C'_m$  and  $\phi$  for the statistical inversion of the subsidence data to compaction data, Eq. (A.5). The green dots are the uniaxial compaction coefficients of all sub-domains of the Groningen field as related to the mean porosity in these sub-domains.

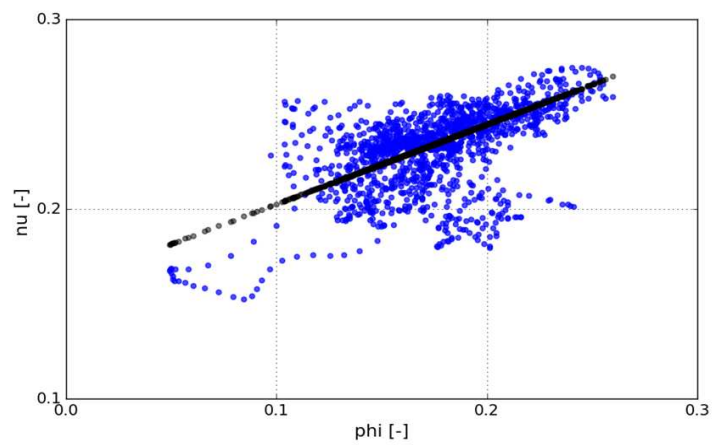


Figure A.3 : Dynamic Poisson ratio versus porosity from the Zeerijp 3a well log (blue dots) derived from P and S waves and density. The black dots show the fit function used for the static Poisson ratio, assuming that the dynamic one is equal to the static one according to Eq. (A.7).

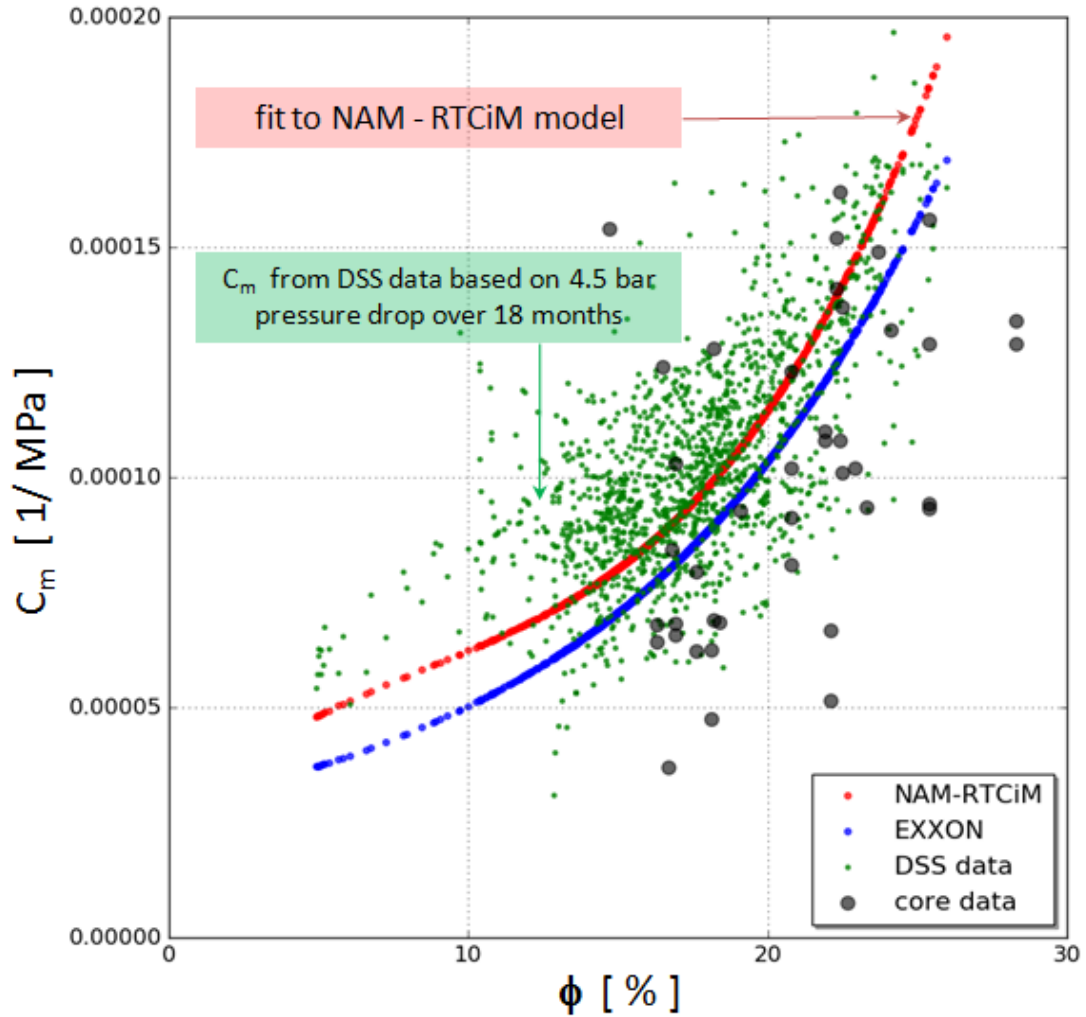


Figure A.4 : Compaction coefficient  $C_m$  as a function of porosity  $\phi$  according to empirical correlations from NAM (red line) and ExxonMobil (blue line), data from Sander Hol c.q. (SGS-I), from cores from the Zeerijp 3a well (black dots), see Hol et al. (2018) and from strain measurements by the distributed strain sensing (DSS) optical fibre cable in the Zeerijp 3a well from Cannon and Kole (2016) (green dots).

The core data and the DSS measurements yield the apparent uniaxial compaction coefficient  $C'_m$ , assuming for the DSS measurements that the reservoir pressure over the period of 18 months monitoring reduced 4.5 bar. Using Eq. (A.6),  $C_m$  is calculated from  $C_m = C'_m/\alpha$  with an estimate for the Biot constant  $\alpha = 0.8$ .

# Appendix B

## Constitutive models for fault failure

In nature, a fault zone encompasses a mm - cm thick fault gouge and herein a micrometers thick fine-grained boundary shear zone or slip layer over which most of the slip takes place. Inside the fault zone, the rock is damaged. Outside the fault zone, rock properties are those of intact rock. Usually, the thickness of the fault gouge and the fine-grained boundary shear zone are small compared to the thickness of a fault zone.

Considering a damaged fault zone of finite thickness, the implementation of constitutive models operating on this fault zone in FEM simulations is as follows. The fault zone in the simulations is a macroscopic construct. On two surfaces at both sides of the fault zone, called in the following the left and right fault surfaces, boundary forces are imposed on the intact rock around them. The boundary forces follow from so-called constitutive models for fault failure in the fault zone. The fault zone is thin compared to other dimensions relevant for the rupture process, such as the reservoir thickness, fault throw or the radius of curvature of the fault zone.

The first type of constitutive models uses that the force of resistance or friction depends on the slip or relative displacement  $D$  [m] between the two surfaces on both sides of the fault zone. Two frequently used examples are the so-called linear strain weakening model where the frictional resistance linearly decreases with  $D$  until the dynamic frictional resistance is reached and the model of Ohnaka (2013) for which strain hardening is preceding strain weakening. The strain hardening is due to non-observable non-elastic deformations on the rough fault surface at various micro-length scales, such as breaking of cohesive bonds between particles, micro-cracking, fracturing of small asperities and ploughing of hard fragments of rock into the other surface.

The second type of models uses that the force of resistance depends on the relative displacement velocity  $\dot{D}$  [m/s]. One example is the rate-and-state friction model, which originates from Dieterich, see for example Dieterich (1979). In this model the resistance also depends on the state of the fault surface after a previous slip event. The results of this empirical model, which explains a number of slip experiments in the laboratory, have been recently explained by a fundamental micro-mechanical model, see Chen and Spiers (2017). This micro-mechanical model is based on inter-granular pressure solution and

granular flow.

Both model types have been implemented in FEM simulations because we have no arguments to prefer one model over the other at this stage. In this report, we use only Ohnaka's model.

The boundary forces on the intact rock follow from algebraic or differential equations in accordance with the selected constitutive model. Firstly, we present equations for the stresses on the fault plane and the algebraic expressions for the friction coefficient according to the linear strain weakening model and according to Ohnaka's strain strengthening/weakening model.

Both models are intended for seismic slip which takes place in fractions of a seconds to several seconds. Since there could be also relatively slow deformations in a fault gouge leading to elastic strain relaxation, we show in §B.4 how a simple strain relaxation model can be added to the constitutive equations.

In §B.5, we explain how relative displacements on the fault plane are calculated from displacements on the left (l) and right (r) surfaces. In the following, all variables used are function of space and time.

## Appendix B.1 Stresses on the fault plane

The tangential stresses on the left and right surfaces of the fault zone are given by

$$\tau_l = \tau_{field} + \text{sign}(D_{tl}) \min[G'_{flt} \text{abs}(D_{tl}), \max(0, \tau_{fric,l})], \quad (\text{B.1})$$

and

$$\tau_r = -\tau_{field} - \text{sign}(D_{tr}) \min[G'_{flt} \text{abs}(D_{tr}), \max(0, \tau_{fric,r})]. \quad (\text{B.2})$$

$\tau_{field}$  [Pa] is the field stress component parallel with the fault zone or in tangential direction.  $G'_{flt} = G_{flt}/w_{flt}$  [Pa/m] is the stiffness of the fault zone in tangential direction.  $w_{flt}$  [m] is the width of the fault zone.  $G_{flt} = \mu_{flt}$  [Pa] is the shear modulus of the fault zone.  $D_{tl}$  and  $D_{tr}$  [m] are components of the relative displacements calculated for the left and right surfaces during the period of reservoir compaction and during fault rupture;  $D_{tl} = D_{tr}$ . The components are parallel with the fault zone, i.e., in tangential direction.

The second terms of the RHS of these equations follow from the elastic or non-elastic deformation of the fault zone during reservoir compaction and during rupture. For the left surface, for small displacements and for  $D_{tl} \rightarrow 0$ , the elastic stress  $G_{flt}|D_{tl}|$  applies until the elastic stress exceeds the frictional resistance  $\tau_{fric,l}$ . The frictional stresses on the left and right surfaces of the fault zone are given by

$$\tau_{fric,l} = \mu_{ll} \text{abs}(\sigma'_{nl}), \quad (\text{B.3})$$

and

$$\tau_{fric,r} = \mu_{rr} \text{abs}(\sigma'_{nr}). \quad (\text{B.4})$$

$\sigma'_{nl}$  and  $\sigma'_{nr}$  [Pa] are the normal stresses on the left and right surfaces of the fault zone.  $\mu_{ll} = \mu_{ll}(D_{tl})$  and  $\mu_{rr} = \mu_{rr}(D_{tr})$  [-] are the friction coefficients on these surfaces. The normal stresses depend on the relative normal displacements as

$$\sigma_{nl} = \sigma'_{field} + E'_{flt} D_{nl} \quad \text{and} \quad \sigma_{nr} = \sigma'_{field} + E'_{flt} D_{nr}. \quad (\text{B.5})$$

$\sigma'_{field}$  [Pa] is the effective normal stress on the fault following from the field stress.  $E'_{flt} = E_{flt}/w_{flt}$  [Pa/m] is the stiffness of the fault zone in the normal direction to the fault zone.  $E_{flt}$  [Pa] is the mean Young modulus in the fault zone.  $D_{nl}$  and  $D_{nr}$  [m] are the relative displacement components normal to the fault zone for the left and right surfaces during the period of reservoir compaction and during fault rupture;  $D_{nl} = D_{nr}$ .

The fault stiffnesses in normal and tangential directions,  $E'_{flt}$  and  $G'_{flt}$  are proportional to the inverse of the width of the fault zone  $w_{flt}$ . Doing so, the constitutive equations shown below and related input parameters do not significantly depend on  $w_{flt}$ <sup>1</sup>. We use  $w_{flt} = 1$  m. Comparable results are found for other values  $w_{flt}$  of the same order.

There is no data about the in-situ mechanical properties of the fault zones in the Rotliegend sandstone in the field. At this stage, we calculate the Young and shear moduli of the fault zone from weighted averages of the Young and shear moduli of the intact rock on both sides of the fault zone. At a specific location along the fault zone, the moduli on both sides of the fault zone differ because of fault throw. Taking weighted averages,

$$E_{flt} = \frac{2E_{flt,l}E_{flt,r}}{E_{flt,l} + E_{flt,r}}, \quad (\text{B.6})$$

and

$$G_{flt} = \frac{2G_{flt,l}G_{flt,r}}{G_{flt,l} + G_{flt,r}}. \quad (\text{B.7})$$

$E_{flt,l}$  and  $E_{flt,r}$  are the Young moduli and  $G_{flt,l}$  and  $G_{flt,r}$  are the shear moduli of intact rock on the left and right sides of the fault zone, respectively. The Poisson ratio of the fault zone follows from  $E = 2(1 + \nu)G$  or

$$\nu_{flt} = \frac{E_{flt}}{2G_{flt}} - 1. \quad (\text{B.8})$$

The expressions used for the normal and shear stress on the fault due to field stresses and the reservoir pressure  $p$  [Pa] are, see Fjaer et al. (2008), §1.1.3,

$$\sigma'_n = \frac{\sigma_v + \sigma_h}{2} + \frac{\sigma_h - \sigma_v}{2} \cos(2\theta) - p, \quad (\text{B.9})$$

---

<sup>1</sup>If  $w_{flt}$  would be very small and the Young and shear moduli in the fault zone would be of the same order as those of the intact rock at both sides of the fault zone, numerical convergence problems may arise as high stresses would be generated by very small displacements.

and

$$\tau = \frac{\sigma_v - \sigma_h}{2} \sin(2\theta). \quad (\text{B.10})$$

$\sigma_v$  and  $\sigma_h$  [Pa] are the vertical and horizontal field stresses.  $\theta = \delta$  [rad] is the angle which the normal of the fault plane makes with the horizontal plane. For numerical reasons, we have reduced the shear stress to zero at the lower end of the fault, deep into the Carboniferous and at the upper end of the fault, deep into the Zechstein. This artifact has no effect on fault instability and rupture in the reservoir.

## Appendix B.2 Linear strain weakening model

For the linear strain weakening model, the friction coefficient  $\mu$  [-] depends on the relative displacement in tangential direction  $D_t$  [m], i.e.,

$$\mu = \mu_r + (\mu_s - \mu_r) \frac{D_t}{D_c} \quad \text{for } D_t < D_c \quad \text{and} \quad \mu = \mu_r \quad \text{for } D_t \geq D_c. \quad (\text{B.1})$$

In Comsol<sup>TM</sup>, for the left fault surface,

$$\mu_{ll} = \max(\mu_r, \mu_r + (\mu_s - \mu_r)(1 - D_{fric,tl}/D_c)), \quad (\text{B.2})$$

and for the right fault surface,

$$\mu_{rr} = \max(\mu_r, \mu_r + (\mu_s - \mu_r)(1 - D_{fric,tr}/D_c)). \quad (\text{B.3})$$

$\mu_s$  [-],  $\mu_r$  [-] and  $D_c$  [m] are the static and dynamic or residual friction coefficients and the so-called critical slip or critical breakdown relative displacement, respectively. These input parameters must be determined from laboratory experiments or field observations.

For the linear strain weakening model the input parameters  $D_c$ ,  $\mu_s$  and  $\mu_r$  relate to the so-called slip-weakening ‘rate’ parameter<sup>2</sup>  $W$  [Pa/m] relevant for the onset of instability, see also van den Bogert (2018b), i.e.,

$$W = \frac{\sigma'_n(\mu_s - \mu_r)}{D_c}. \quad (\text{B.4})$$

According to Uenishi and Rice (2003), there is a universal length  $L_{nuc}$  [m] for slip weakening fault instability. For the linear slip weakening model, the nucleation of a slip weakening instability under a locally peaked, increasing stress field has been investigated by solving an eigenvalue problem in two dimensions for quasi-static elastic equilibrium. Dynamic effects related to rock inertia are not included in this problem. The critical length relevant to instability can be expressed in terms of the smallest eigenvalue, shear modulus and  $W$ , i.e.,

$$L_{nuc} = c \frac{\mu}{W(1 - \nu)} \quad \text{where } c = 1.158, \quad (\text{B.5})$$

---

<sup>2</sup>The name ‘rate’ is a bit confusing here because it is not related to a variable that changes with time.

or vice-versa,

$$\frac{D_c}{L_{nuc}} = \frac{1}{c(1-\nu)} \frac{\mu}{\sigma'_n(\mu_s - \mu_r)}. \quad (\text{B.6})$$

According to three dimensional numerical rupture modelling for various shaped nucleation patches by Galis et al. (2015), nucleation occurs when the area of the nucleation patch  $A$  [m<sup>2</sup>] exceeds a value

$$A_{nuc} = (3.82 + 1.75S^{2.81})L_c^2 \quad \text{where} \quad L_c = \frac{\mu D_c}{\sigma'_n(\mu_s - \mu_r)} \quad \text{and} \quad S = \frac{\mu_s - \mu_0}{\mu_0 - \mu_r}. \quad (\text{B.7})$$

The dimensionless stress parameter  $S$  [-] ratio compares the stress condition on the fault plane outside the nucleation patch at the onset of fault instability,  $\tau_0 = \sigma'_n \mu_0$  [Pa] to the static and dynamic stresses. When the region outside the patch is critically loaded and close to instability  $S \rightarrow 0$  and the nucleation patch required for rupture is the smallest. The results are obtained for simulations using a Poisson ratio in the rock  $\nu = 0.25$ .

For  $S \rightarrow 0$  and for a circular nucleation patch, Eq. (B.7) can be rewritten as, using  $L_{nuc} = \sqrt{4/\pi} \sqrt{A_{nuc}}$ ,

$$\frac{L_{nuc}}{D_c} = \sqrt{\frac{3.82\pi}{4}} \frac{\mu}{\sigma'_n(\mu_s - \mu_r)}. \quad (\text{B.8})$$

For  $\nu = 0.25$ , the pre-factors in Eqs. (B.7) and (B.8) are 1.2 and 1.7, respectively. The difference is due to the different problems solved. Eq. (B.7) follows from a solution in two dimensions, Eq. (B.8) follows from a solution in three dimensions.

For a shear modulus  $\mu = 6$  GPa, effective normal stress  $\sigma'_n = 10$  MPa,  $\mu_s - \mu_r = 0.3$  and a critically stressed fault zone  $S \rightarrow 0$ , we have  $L_{nuc} \sim 300D_c$ . For a typical value  $D_c = 0.01$  m, a nucleation patch  $L_{nuc} \sim 3$  m is sufficient to cause a rupture of the critically stressed fault zone. According to Eq. (B.7), for a less stressed fault zone with  $S = 1$ , the size of the nucleation patch increases with about 20%.

### Appendix B.3 Ohnaka's model

As for the linear strain weakening model, the friction coefficient  $\mu$  depends only on the relative displacement in tangential direction. For the left fault zone surface,

$$\mu_{ll} = \mu_r + (\mu_s - \mu_r)(1 + \alpha \log(1 + \beta D_{fric,tl})) \exp(-\eta D_{fric,tl}), \quad (\text{B.1})$$

and for the right fault zone surface,

$$\mu_{rr} = \mu_r + (\mu_s - \mu_r)(1 + \alpha \log(1 + \beta D_{fric,tr})) \exp(-\eta D_{fric,tr}). \quad (\text{B.2})$$

$\mu_s$  [-],  $\mu_r$  [-] are the static and dynamic or residual friction coefficients.  $\alpha$  [-] and  $\beta$  [1/m] are input parameters related to the increase of friction or strength when there is strain

strengthening for relatively small displacements.  $\eta \propto 1/D_c$  [ $\text{m}^{-1}$ ] is an input parameter, like the critical slip or critical breakdown relative displacement, which determines the subsequent decrease of frictional resistance with displacement, see Ohnaka (2013), §2.2. These input parameters must be determined from laboratory experiments or constrained by field observations.

## Appendix B.4 Creep in the fault gouge

During the compaction of the reservoir in the Groningen field, relatively slow non-elastic deformation in the thin fault gouge of a fault zone may take place due to changes in the shear stress evolving from gas production, in particular where local shear stresses are high.

Geomechanical measurements on cores from the Zeerijp 3a well indicate that there is significant non-elastic deformation during compaction, see Hol et al. (2018). Also, compaction models used for subsidence, like the RTCiM model, need non-elastic time relaxation effects to match the observed subsidence above the Groningen field with the reduction of the reservoir pressure over time<sup>3</sup>.

These slow non-elastic deformations including those from tectonic stresses over geological time, e.g. due to glacial rebound or due to creep in the overlying Zechstein salt formation, are supposed not to contribute to the slip  $D$  in the constitutive models for seismic slip presented in the previous sections. Further,  $D = 0$  is supposed at the start of gas production. Only the elastic stress generated by compaction is relevant for seismic slip.

A possibility to subtract relatively slow non-elastic deformation from the total deformation in the fault gouge is by adding two ordinary differential equations for strain relaxation to the constitutive model with an effect on the friction coefficient. For the relative displacement component in tangential direction, calculated on the left and the right surfaces of the fault zone,

$$\frac{d}{dt}D_{creep,tl} = \frac{D_{tl} - D_{creep,tl}}{t_{creep}}, \quad (\text{B.1})$$

and

$$\frac{d}{dt}D_{creep,tr} = \frac{D_{tr} - D_{creep,tr}}{t_{creep}}. \quad (\text{B.2})$$

$t_{creep}$  [s] is a time constant, determining the non-elastic displacement rate in tangential

---

<sup>3</sup>On the other hand, recent micro-structural investigation of intact sandstone cores recovered from the Stedum-1 well before gas production and recovered from the Zeerijp-3a well after gas production by Bart Verberne c.q. (Earth materials group of Chris Spiers, university of Utrecht, the Netherlands) shows that there is no evidence for gas production-induced grain-scale crystal plastic yielding, dissolution at grain contacts, inter- or intra-granular cracking and grain rearrangement. The mechanisms controlling gas production-induced compaction did not leave micro-structural indicators of non-elastic deformation in the cores investigated. It is debated whether the Stedum-1 well cores, preserved over 60 years in the core shed, can be used for this purpose.

direction. For  $t_{creep} \rightarrow \infty$ , creep is negligible.  $D_{tl}$  and  $D_{tr}$  [m] are the relative displacement components in tangential direction, defined below. The relative displacement components  $D_{fric,tl}$  and  $D_{fric,tr}$ , used in the expressions for the friction coefficients, are calculated from

$$D_{fric,tl} = D_{tl} - D_{creep,tl}, \quad (\text{B.3})$$

and

$$D_{fric,tr} = D_{tr} - D_{creep,tr}. \quad (\text{B.4})$$

In this report, little creep has been used to trigger the tremor at the required reservoir pressure.

## Appendix B.5 Mapping displacements from one fault surface to the second fault surface on the other side of the fault zone

In the finite element model used in COMSOL<sup>TM</sup>, constitutive models for the fault zone can be defined by a set of algebraic or ordinary differential equations operating on two fault surfaces at both sides of the fault zone. These surfaces follow the macroscopic curvature of the fault zone or fault plane. The distance between them is small compared to the length scales, related to fault throw, reservoir thickness or length scales related to the curvature of the fault zone. In the following, the two surfaces on both sides of the fault zone are called the left (l) and right (r) surfaces. The equations are given for three dimensions.

To calculate the relative displacements between two fault surfaces, the values of the displacements  $\mathbf{u} = (u, v, w)$  in  $(x, y, z)$  directions<sup>4</sup> on one fault plane are mapped on corresponding coordinates of the other fault plane by using the so-called linear extrusion coupling in COMSOL<sup>TM</sup>. For calculations on the left fault surface, the normal displacement  $u_{nl}$  is

$$u_{nl} = u_l e_{n1l} + v_l e_{n2l} + w_l e_{n3l}. \quad (\text{B.1})$$

$\mathbf{u}_l = (u_l, v_l, w_l)$  [m] is the displacement vector on the left fault plane.  $\mathbf{e}_{nl} = (e_{n1l}, e_{n2l}, e_{n3l})$  [-] is the unit vector in the normal direction of the boundary coordinate system of the left fault plane. The normal displacement on the right fault plane after extrusion to the left fault plane is

$$\tilde{u}_{nr} = \tilde{u}_r e_{n1r} + \tilde{v}_r e_{n2r} + \tilde{w}_r e_{n3r}. \quad (\text{B.2})$$

$\mathbf{e}_{nr} = (e_{n1r}, e_{n2r}, e_{n3r})$  [-] is the unit vector in the normal direction of the boundary coordinate system of the right fault plane.  $\tilde{\mathbf{u}}_r = (\tilde{u}_r, \tilde{v}_r, \tilde{w}_r)$  is the extruded displacement at the corresponding fault zone coordinates on the right fault plane. Since the normal

---

<sup>4</sup>Usually, in three dimensional simulations, the z-direction is along depth and in two dimensional simulations, the y-direction is along depth.

vectors on both fault planes point towards each other, the relative normal displacement  $D_{nl}$  [m] calculated for the left plane is

$$D_{nl} = -\tilde{u}_{nr} - u_{nl}. \quad (\text{B.3})$$

$D_{nl}$  is positive if the distance between the two fault planes increases.

For the left fault plane, the tangential components of the displacement in the orthogonal directions 1 and 2 are

$$u_{t1l} = u_l e_{t11l} + v_l e_{t12l} + w_l e_{t13l} \quad \text{and} \quad u_{t2l} = u_l e_{t21l} + v_l e_{t22l} + w_l e_{t23l}. \quad (\text{B.4})$$

$\mathbf{e}_{t1l} = (e_{t11l}, e_{t12l}, e_{t13l})$  and  $\mathbf{e}_{t2l} = (e_{t21l}, e_{t22l}, e_{t23l})$  [-] are the unit vectors in tangential directions 1 and 2 of the boundary coordinate system of the left fault plane, respectively. The corresponding tangential displacements on the right fault plane after extrusion to the left fault plane are

$$\tilde{u}_{t1r} = \tilde{u}_r e_{t11r} + \tilde{v}_r e_{t12r} + \tilde{w}_r e_{t13r} \quad \text{and} \quad \tilde{u}_{t2r} = \tilde{u}_r e_{t21r} + \tilde{v}_r e_{t22r} + \tilde{w}_r e_{t23r}. \quad (\text{B.5})$$

$\mathbf{e}_{t1r} = (e_{t11r}, e_{t12r}, e_{t13r})$  and  $\mathbf{e}_{t2r} = (e_{t21r}, e_{t22r}, e_{t23r})$  [-] are the unit vectors in the tangential directions 1 and 2 of the boundary coordinate system of the right fault plane. In the case that the tangential unit vectors for direction 1 on both fault planes are parallel to each other,

$$D_{t1l} = u_{t1l} - \tilde{u}_{t1r}. \quad (\text{B.6})$$

Similar equations hold for the relative displacement or slip  $D_{t2l}$  and relative displacements calculated for the right surface. The total slip in tangential direction, relevant for a change in the friction coefficient, is given by

$$D_{tl} = \sqrt{D_{t1l}^2 + D_{t2l}^2}. \quad (\text{B.7})$$

Similar expressions hold for relative displacement velocities, making use of the variables  $(ut, vt, wt)$  in COMSOL<sup>TM</sup>. For two dimensional calculations, the equations for two tangential components reduce to equations for one tangential component making use of the variables  $(u, v)$  and  $(ut, vt)$  in  $(x, y)$  directions where the y-axis is along depth.

# Appendix C

## Breakdown stress drop

In this appendix, we show a few expressions from the literature which relate the breakdown stress drop  $\Delta\tau$  to the seismic moment and slip plane dimensions. The slip plane dimensions can be derived from the displacement spectra of the ground motions and/or from the apparent source time functions of the tremor.

This has been done for the Zeerijp  $M_L$  3.4 tremor, see Wentinck (2018a). This study indicates that the slip plane is not very elongated along fault strike, with the largest dimension  $L$  not exceeding 0.4 km. Combined with the results of 2D dynamic rupture modelling, as presented in this report, we believe that the rupture plane is more or less equi-dimensional.

The mean low corner frequency of the Zeerijp tremor  $f_c \sim 3$  Hz. The corner frequencies of the two other large tremors in the Groningen field of similar magnitude, i.e., the Westeremden  $M_L$  3.5 tremor of 2006 and the Huizinge  $M_L$  3.4 tremor of 2012 are about 1.9 Hz and 2.1 Hz, respectively<sup>1</sup>. Having similar magnitudes, the two older tremors seem to have larger slip areas and a smaller breakdown stress drop.

### Appendix C.1 Breakdown stress drop

The relation between the seismic moment, shear modulus of the rock, slip area and slip is given by

$$M_0 = \mu S D \quad \text{where} \quad S = WL, \quad (\text{C.1})$$

and vice-versa,

$$D = \frac{M_0}{\mu S}. \quad (\text{C.2})$$

---

<sup>1</sup>The Huizinge tremor of August 12 in 2012 has in the KNMI catalogue a moment magnitude  $M = 3.6$ . According to Dost and Kraaijpoel (2013), the best estimate for the local magnitude of this tremor is  $M_L = 3.4$ . According to Dost et al. (2018), the best correlation between  $M_L$  and  $M$  is  $M = M_L$  for  $M > 2.5$ .

$M_0$  [J] is the seismic moment<sup>2</sup>,  $\mu$  [Pa] is the shear modulus,  $S$  [m<sup>2</sup>] is the slip area and  $D$  [m] is the average slip.  $W$  [m] and  $L$  [m] are the width and the length of an approximately rectangular slip plane, respectively. According to Leonard (2010), it is generally accepted that the seismic moment  $M_0$  of natural earthquakes scales with the slip area  $S$  [m<sup>2</sup>] as  $M_0 \propto S^{3/2}$ . This holds also for considerable aspect ratio's  $L/W$ . According to Eq. (C.2), this implies that the slip length scales as  $D \propto S^{1/2}$ .

The part of the shear stress on the fault plane which is released by the rupture, or the breakdown stress drop  $\Delta\tau$  [Pa], follows from

$$\Delta\tau = c \frac{M_0}{SL_c}. \quad (\text{C.3})$$

$L_c$  is a characteristic rupture dimension that is normally considered to be the smallest spatial dimension of the rupture plane and  $c$  is a constant that depends on the geometry of the slip plane. Theoretical expressions have been derived for the constant  $c$ . For a circular plane with radius  $R$  [m] and a Poisson ratio  $\nu = 0.25$  from a static model, see Udias et al. (2014), §9.4,

$$D = \frac{16}{7\pi} \frac{\Delta\tau}{\mu} R. \quad (\text{C.4})$$

Combining this with Eq. (C.2), we have, see also Scholz (2002), Eq. 4.30 or Leonard (2010), Eq. 1,

$$\Delta\tau = c \frac{M_0}{\pi R^3} \quad \text{where} \quad c = \frac{7\pi}{16} \sim 1.4. \quad (\text{C.5})$$

For a square plane with the same area as the circular plane and slip along dip, according to Leonard (2010), Eq. 3, using  $L_c = W = L$  and  $W^2 = \pi R^2$ ,

$$\Delta\tau = c \frac{M_0}{W^2 L} = c \frac{M_0}{\pi R^3} \quad \text{where} \quad c = \frac{4(\lambda + \mu)}{\pi(\lambda + 2\mu)}. \quad (\text{C.6})$$

$\lambda$  and  $\mu$  [Pa] are the first and second Lamé parameters. The second Lamé parameter is equal to the shear modulus. For reservoir rock with  $\lambda = 4.2$  GPa and  $\mu = 6.2$  GPa,  $c \sim 0.8$ . According to Stein and Wysession (2003), §4.6.3, Eq. 20, using  $W = L$  and  $W^2 = \pi R^2$ ,

$$\Delta\tau = \frac{8}{3\pi} \frac{M_0}{WL^2} = c \frac{M_0}{\pi R^3} \quad \text{where} \quad c = \frac{8}{3\pi} \sim 0.85. \quad (\text{C.7})$$

Considering present uncertainties about the shape of the slip plane and the approximations

---

<sup>2</sup>According to Dost et al. (2018), the moment magnitude  $M$  [Richter] is about equal to the local magnitude  $M_L$  [Richter]. Using  $M_L = M \sim 3.4$  and Kanamori's relation between seismic moment  $M_0$  [J] and moment magnitude  $M$  [Richter], i.e.,  $\log M_0 = 3/2(M + 6.07)$ , the corresponding seismic moment  $M_0$  of the tremor is  $M_0 = 160$  TJ.

made in the theoretical models, we use  $c \sim 1$ . According to Eq. (C.4), the average slip  $D$  scales to the slip plane radius as  $D/R \sim \Delta\tau/\mu$ . For  $\tau = 4$  MPa and  $\mu = 6$  GPa,  $D/R \sim 0.0005$ . For  $R = 0.25$  km,  $D \sim 0.1 - 0.2$  m.

# Appendix D

## Other simulation results

We show below additional results of simulation A and simulation B with another stress condition on the fault due to another fault dip angle. Hereafter, we show a few figures of so-called source time functions that can be derived from these simulations.

To illustrate what can be expected from dynamic rupturing in three dimensions, we show an example in §D.4.

### Appendix D.1 Additional results of simulation A

Figure D.1 shows the vertical displacement in the reservoir due to compaction and due to rupture. The bending of the iso-displacement filled contours around the fault immediately shows how the shear stress due to compaction builds up. The displacements following from rupture show that the rock on the left part of the faults moves upwards and on the right side moves downwards. A downwards vertical displacement of  $\sim 0.6$  m away from the fault zone agrees with an average compaction coefficient  $C_{m,ave} \sim 1.1 \cdot 10^{-4} \text{ MPa}^{-1}$  and an average porosity over the reservoir of about 18%, see Figure A.4 in Appendix A<sup>1</sup>.

Figure D.2 shows the normal relative displacement  $D_n$  [m] and the normal effective stresses on the fault plane  $\sigma'_n$  before and after rupture. Compared to changes in the tangential stress, those in the normal effective stress are small.

Figure D.3 shows the friction coefficient before, during and after rupture. During rupture, the friction coefficient  $\mu$  first increases to a maximum value of about 0.8, consistent with Ohnaka's constitutive model used, see Figure 2.6. At the rupture front, it steeply drops to  $\mu_r$ .

The maximum mean rupture front velocity in the less stressed parts of the fault plane during the time intervals shown is  $V_r \sim 1$  km/s. This value is considerably smaller than 80 - 90% of the shear velocity of 2.2 km/s, which is normally used for the rupture velocity. A

---

<sup>1</sup>This value follows from  $C_{m,ave} = \Delta h/h/(\alpha\Delta p)$  and using  $\Delta h \sim -0.6$  m,  $h = 270$  m,  $\alpha = 0.8$  and  $\Delta p = -26$  MPa.

similar maximal  $V_r$  in downwards direction can be derived from the displacement contour lines at 10 ms time intervals in Figure 3.3 .

The maximum rupture velocity depends on the shear stress on the fault outside the nucleation zone and accidental circumstances leading to more nucleation patches. Figure D.4 shows an example for rock failure according to Ohnaka's model but without strain hardening. The parameters used lead to a rupture at the same reservoir pressure of 9 MPa. They are  $\mu_s = 1.1$ ,  $\mu_r = 0.2$ ,  $\alpha = 0$  and  $\eta = 365 \text{ m}^{-1}$  ( $D_{c,equiv} \sim 13.7 \text{ mm}$ ), see the dashed magenta line in Figure 2.6 . Both curves have a comparable slip-weakening rate parameter  $W$ , see Appendix B, Eq. (B.4). In this case, the nucleation starts in the upper part of the reservoir. Due to stress redistribution, a second nucleation starts 0.1 s later in the centre of the reservoir.

Figure D.5 shows the horizontal and vertical displacements in the rock surrounding the fault and the rotational motion of the fault plane  $M_{rot,flt}$  [ $\text{m}^2$ ] following from seismic slip or rupture.  $M_{rot,flt}$  is an integral over the two surfaces on both sides of the fault zone of displacement moments of fault zone elements with length  $ds$ . For displacements  $(u, v)$  of fault zone elements on both surfaces, because of rupture,

$$M_{rot,flt} = \int_{flt} (x'v - z'u) ds. \quad (\text{D.1})$$

$(x', z')$  are the relative coordinates of the fault zone elements with respect to the centre coordinates of the fault  $(x_{cen,flt}, z_{cen,flt})^2$ . The rotational motion due to (tangential) slip along the fault zone is

$$M_{rot,flt,t} = \int_{flt} (x'v \cos(\theta) - z'u \sin(\theta)) ds. \quad (\text{D.2})$$

$\theta$  [degrees] is equal to the dip angle of the fault  $\delta$ . The figure of the rotational motions  $M_{rot,flt}$  and  $M_{rot,flt,t}$  versus time shows that during rupture the fault rotates more than would be expected from slip along the fault. It needs to be sorted out whether the extra rotation contributes to the difference between the dip angle of slip plane derived from seismic inversion of the ground motions and the dip angle of the fault derived from ant-tracking.

---

<sup>2</sup> $x' = x - x_{cen,flt}$  and  $z' = z - z_{cen,flt}$  where  $(x_{cen,flt}, z_{cen,flt})$  are the coordinates of the fault centre. They are geometric means of the coordinates of the top and bottom of the fault and given by  $x_{cen,flt} = (x_{top,flt} + x_{bot,flt})/2$  and  $z_{cen,flt} = (z_{top,flt} + z_{bot,flt})/2$ . The coordinate  $z$  along depth used in this report is the coordinate  $y$  used in Comsol<sup>TM</sup>.

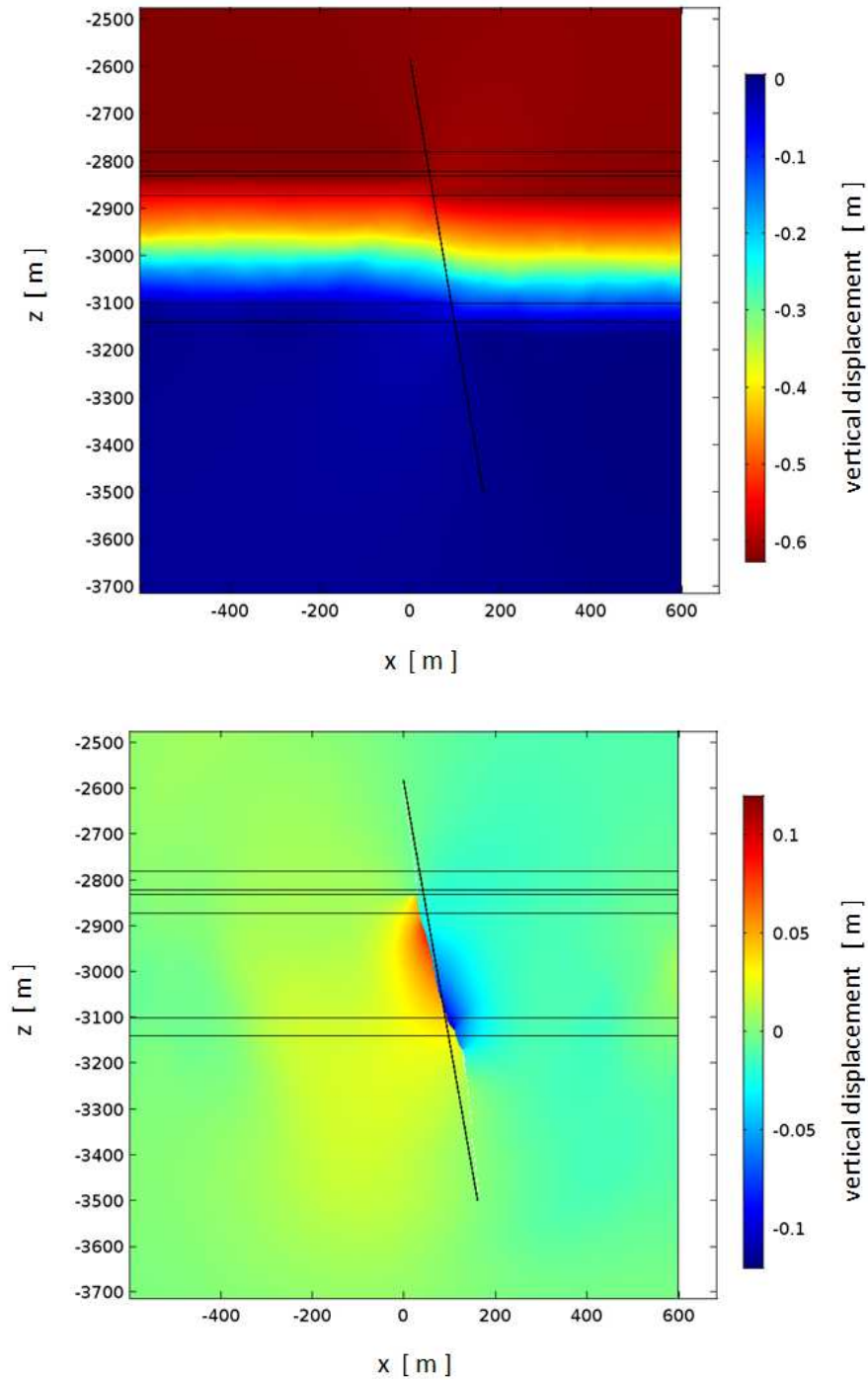


Figure D.1 : Simulation A1: Top figure: vertical displacement due to compaction. Bottom figure: vertical displacement due to rupture.

The bending of the filled contours of iso-displacement around the fault immediately shows how the shear stress due to compaction builds up. The displacement following from rupture shows that the rock on the left part of the faults moves upwards and on the right side moves downwards.

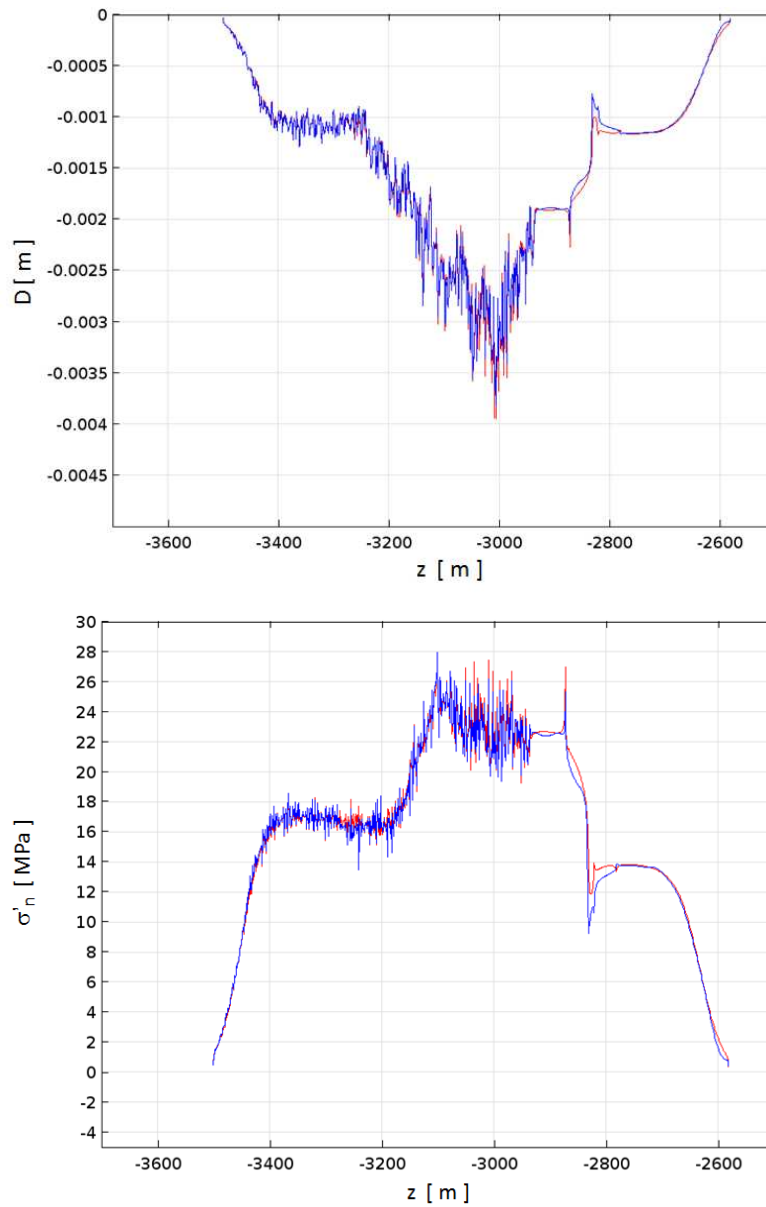


Figure D.2 : Simulation A1: Top figure: normal relative displacement  $D_n$  just before and after rupture. Bottom figure: the effective normal stress  $\sigma'_n$  on the fault just before and after rupture and just after the rupture. The condition before rupture is shown by the red lines, the one after rupture by the blue lines.

Changes in the normal displacement and effective stress on the fault are small when compared to similar changes in tangential direction.

The stresses drop to zero at the upper and lower ends of the fault. This stress reduction is artificial to speed up calculations. It has no effect on the compaction and rupture in the reservoir and in the upper part of the Carboniferous.

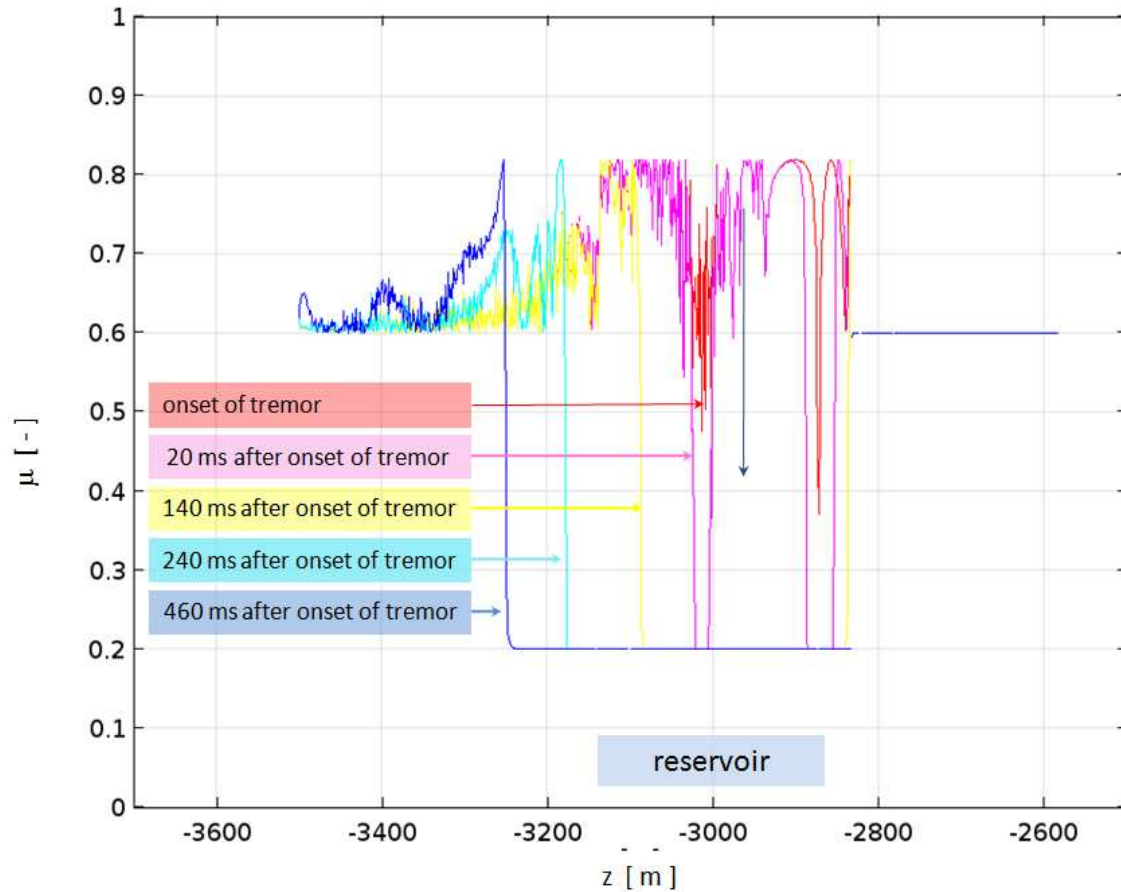


Figure D.3 : Simulation A1: friction coefficient  $\mu$  on the fault plane during rupture. The red line shows the profile at the onset of the tremor. The magenta, yellow, cyan and blue lines show the profiles 20, 140, 240 and 460 ms after the onset of the rupture. The rupture front in the period between 20 - 140 ms after the onset with 0.5 km/s, in the period between 140 - 240 ms after the onset with a mean velocity of 0.9 km/s and in the period between 240 - 460 ms after the onset with a mean velocity of 0.35 km/s downwards. The grid elements are small enough to resolve frictional behaviour at the rupture front. At the rupture front, the friction coefficient firstly increases to a maximum value of about 0.8 consistent with Ohnaka's constitutive model used, see Figure 2.6 .

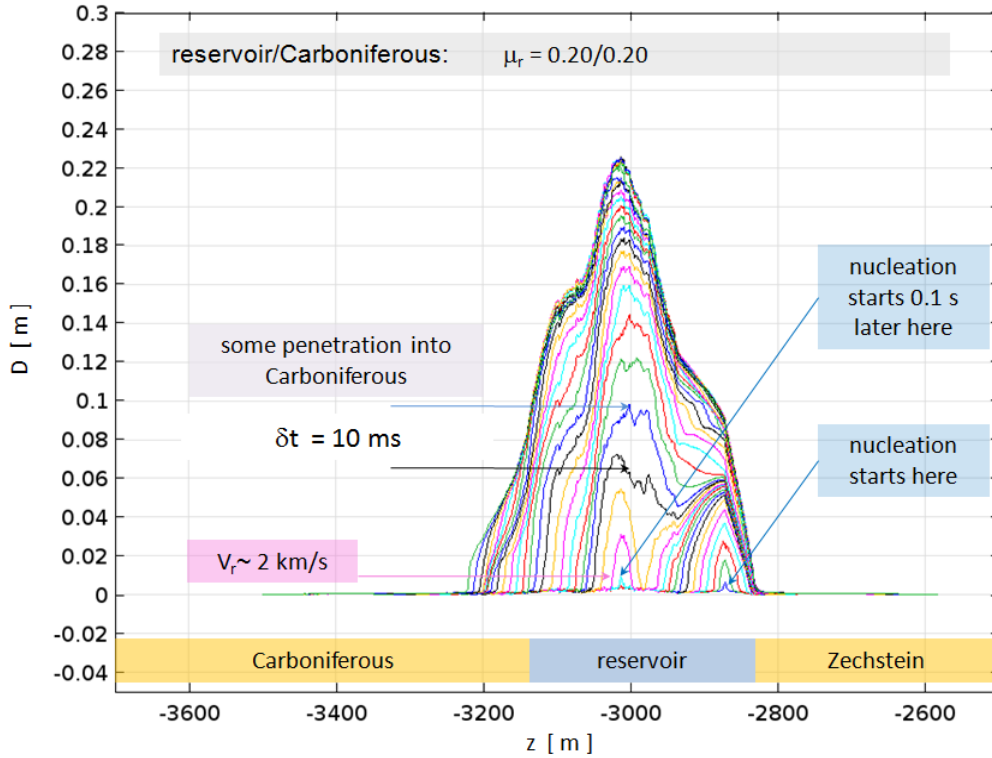


Figure D.4 : Simulation A2: slip or relative displacement  $D_t$  along the fault versus depth during rupture for slip without strain hardening.

The contour lines show snapshots for time steps every 10 ms. In this case, the nucleation starts in the upper part of the reservoir. When the rupture propagates from this location downwards, after about 0.1 s, the rupture nucleates again in the centre of the reservoir. This is followed by a rapid increase of slip between the two nucleation patches. The effect of this rapid increase can clearly be seen in the step increase in the source time function shown in Figure D.9 .

The maximum slip  $D \sim 0.2$  m is comparable with the maximum slip shown in Figure 3.3 . This value is primarily controlled by the residual friction coefficient which is in both cases  $\mu_r = 0.2$ . Also in this simulation, there is penetration of the rupture into the Carboniferous.

The maximum rupture velocity is  $\sim 2$  km/s for a short period (between pink and yellow contour line). The part of the fault plane between these two nucleation patches slips faster than the rest of the fault. This can be concluded from the distance between the contour lines.

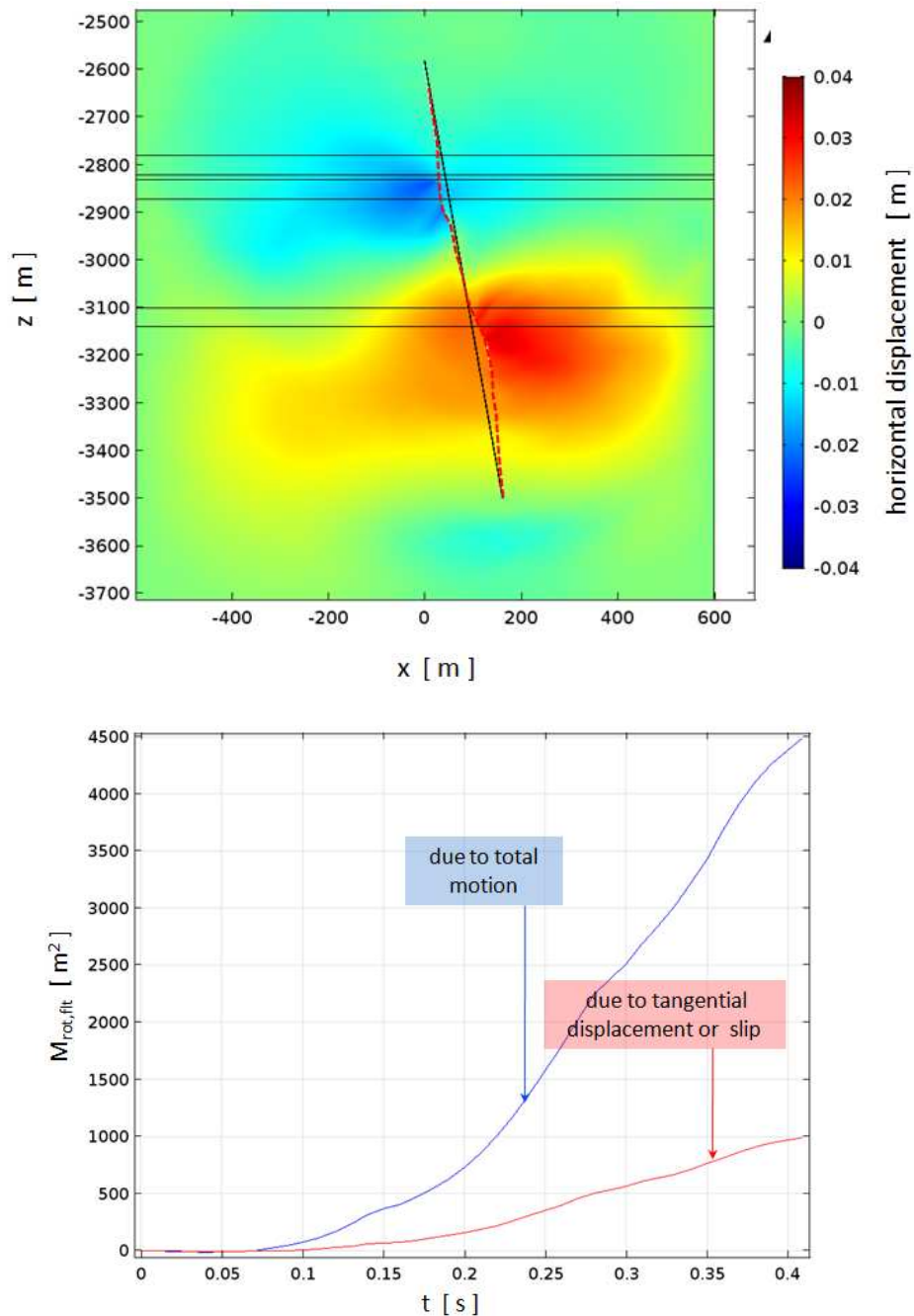


Figure D.5 : Simulation A1: rotation of the fault due to rupture. Top figure: horizontal displacement of the rock surrounding the fault and deformation of the fault plane because of rupture. The red dashed line shows the deformed fault plane after rupture. The vertical displacement is shown in Figure D.1 .

Bottom figure: rotational motions  $M_{rot,flt}$  and  $M_{rot,flt,t}$  versus time during rupture.  $M_{rot,flt}$  (blue line) is the integral of the total displacement moment over the fault surfaces on both sides of the fault zone.  $M_{rot,flt,t}$  (red line) is the integral of the displacement along the fault plane or the (tangential) slip over both sides of the fault zone. The fault plane rotates more than would be expected from slip along the fault plane only.

## Appendix D.2 Results of simulation B

Simulation B is for another stress condition on the fault due to another fault dip angle<sup>3</sup>  $\delta = 75^\circ$ . Again, the focus is on the effect of  $\mu_r$  on the maximum slip and on conditions for rupture propagation into the Carboniferous below the reservoir.

Table 2.3 shows the input parameters. To trigger the rupture at 9 MPa reservoir pressure, the chosen critical breakdown slip  $D_c$  is a bit higher and  $t_{creep}$  two times lower than for simulation A. The residual friction coefficient  $\mu_r$  has been varied to propagate or arrest the rupture in the upper part of the Carboniferous.

Figure D.6 shows the stress conditions before compaction and before rupture. Figure D.7 show the slip during rupture for three cases for which  $\mu_r$  has been varied in the reservoir and in the Carboniferous.

The residual friction coefficient has to be increased from  $\mu_r = 0.20$  to  $\mu_r = 0.30$  to have a comparable slip as in simulation A. This implies that uncertainties in fault dip angle or other shear stresses on the fault considered have a profound effect on the estimation of the drop in the friction coefficient during rupture from combining seismic observations and dynamic rupture modelling. Again, a bit more residual friction in the Carboniferous has a significant effect on the penetration of the rupture into this formation.

---

<sup>3</sup>Additional shear stress could also follow from tectonic stresses but are not considered in this report.

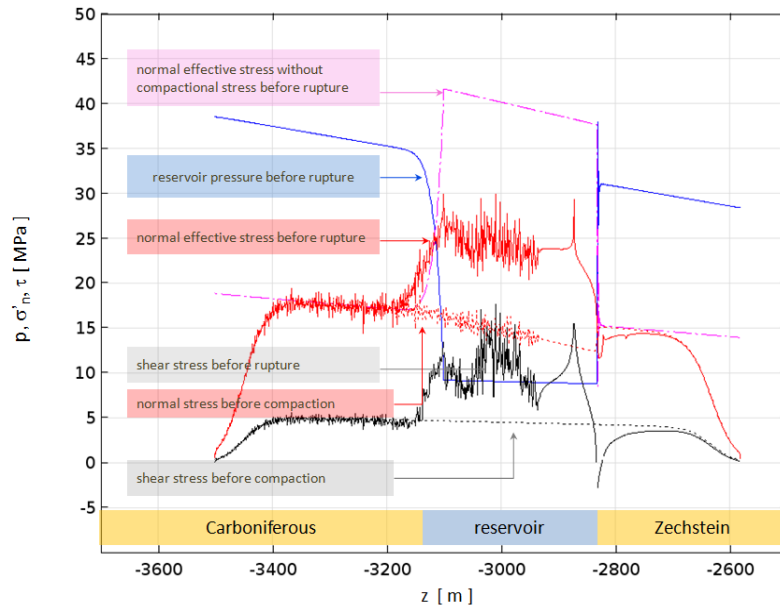


Figure D.6 : Simulation B1: pressure in the reservoir and in the upper part of the Carboniferous and stress on the fault before compaction and before rupture as a function of depth. The black dotted and solid lines show the shear stresses before compaction and just before rupture, respectively. The red dotted and solid lines show the normal effective stresses before compaction and just before rupture, respectively.

The blue line shows that the pressure drop in the reservoir has penetrated into the Carboniferous during a period of almost 60 years. Herewith, the normal effective stress (red line) in the upper part of this formation also increases.

Compared to Figure 3.2 , the shear stress before compaction increases from about 3 MPa to about 5 MPa. Before rupture, it increases from 5 - 10 MPa to 8 - 13 MPa around the centre of the reservoir.

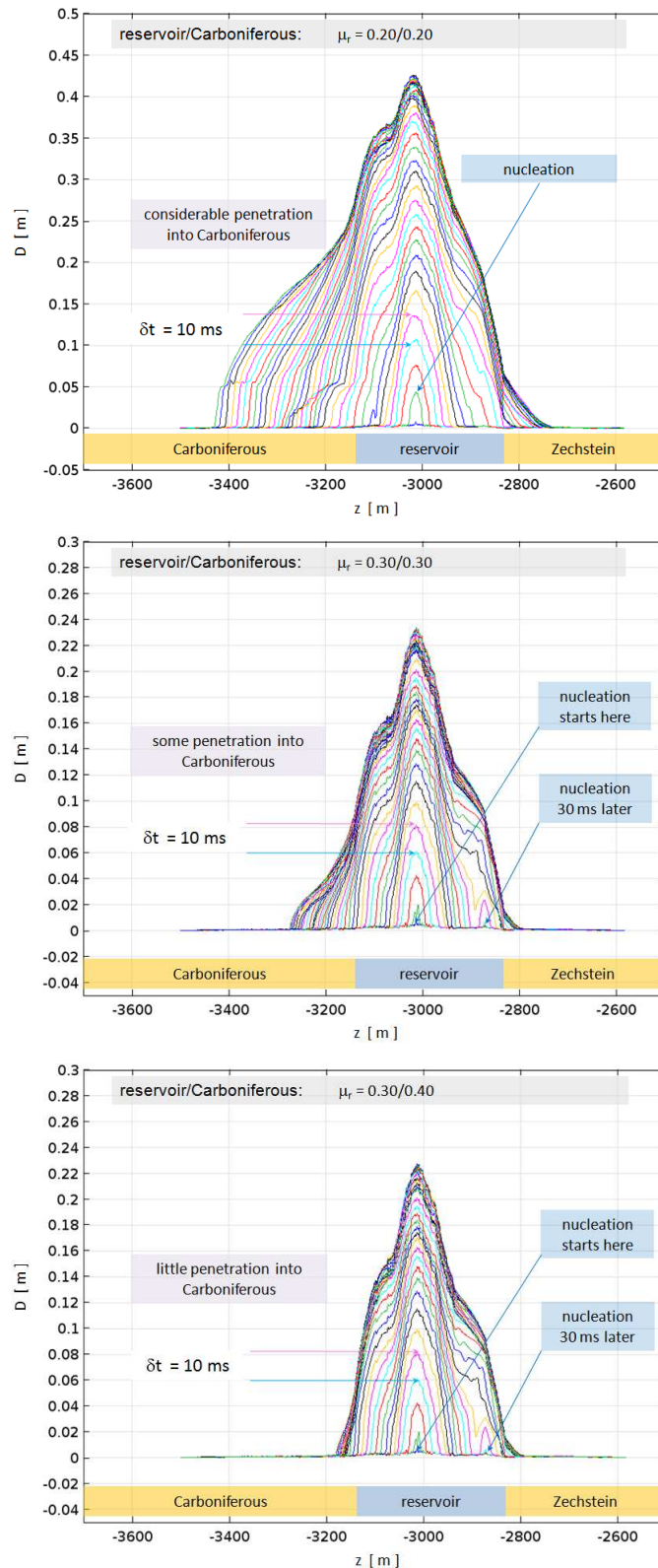


Figure D.7 : Simulations B1, B2 and B3: slip or relative displacement along the fault plane  $D$  during rupture for two values of the residual friction coefficient in the Carboniferous. The fault dip is  $75^\circ$ .

Top figure: simulation B1,  $D_{c,equiv} = 7.5$  mm and  $\mu_r = 0.2$  in reservoir and Carboniferous. Note that the maximum scale along the y-axis is increased from  $D = 0.3$  to  $D = 0.5$  m. The rupture penetrates into the Carboniferous.

Centre figure: simulation B2,  $D_{c,equiv} = 7.3$  mm and  $\mu_r = 0.3$  in reservoir and Carboniferous. Bottom figure: simulation B3,  $D_{c,equiv} = 7.3$  mm and  $\mu_r = 0.3$  in reservoir and  $\mu_r = 0.4$  in Carboniferous.

## Appendix D.3 Source time functions

At a relatively far distance from the tremor epicentre, a seismic source can be modelled as a point source. For a point source, the dimensions of the slip plane and the rupture velocity are indistinguishable and implicitly included in the dynamics of the so-called source time function.

For a point source, the time dependent moment tensor  $\mathbf{M} = \mathbf{M}(t)$  [N] can be factorised in a unit moment tensor  $\mathbf{m}$  [-] and a source time function  $M_0(t)$  [N]. The unit moment tensor  $\mathbf{m}$  [-] is constructed from the unit vectors defining the orientation of the rupture plane and the slip direction, see e.g. Aki and Richards (2009), §3.3. So,

$$\mathbf{M}(t) = \mathbf{m}M_0(t). \quad (\text{D.1})$$

Using the mean relative displacement or slip  $D = D(t)$  over the slip plane as the time-dependent variable and the general relation between slip and seismic moment  $M_0 = \mu SD$ , the seismic moment changes with time as

$$M_0(t) = \mu SD(t) = M_0 f(t) \quad \text{where} \quad D(t) = D_{max} f(t) \quad \text{and} \quad M_0 = \mu SD_{max}. \quad (\text{D.2})$$

$D_{max}$  [m] is the maximum value of the mean slip over the slip plane over time.  $S$  [m<sup>2</sup>] is the surface of the slip plane and  $\mu$  [Pa] the shear modulus of the rock.  $f(t)$  [-] is the dimensionless source time function.

In the far field, the displacements recorded by the seismometers are proportional to  $\dot{M}_0 = dM_0(t)/dt$  or, using Eq. (D.2), proportional to  $\dot{f}(t)$  or  $\dot{D}(t)$ . From two-dimensional dynamic rupture modelling, we can calculate the mean displacement  $D$  over the slip plane as a function of time by integrating the local slip over the slip plane and herewith calculate the mean slip velocity  $\dot{D}(t)$ , i.e.,

$$\dot{D}(t) = \frac{1}{L_{slip}} \int_{flt} \dot{D}(s, t) ds. \quad (\text{D.3})$$

$L_{slip}$  [m] the length of slip plane.

On the other hand, we have derived so-called apparent source time functions  $f_{app}(t)$  [-] from the observed displacements recorded at stations around the Zeerijp tremor epicentre. Of all small tremors with a hypocentre close to the hypocentre of the Zeerijp  $M_L$  3.4 tremor, the  $M_L$  1.7 tremor of December 22 in 2017, has a similar focal mechanism as the  $M_L$  3.4 tremor. Using the observed displacements from the  $M_L$  1.7 tremor, we have derived  $f_{app}(t)$  of the Zeerijp tremor using the method of empirical Green functions.

The idea behind this method is that the source time function  $f_S(t)$  of a small tremor can be regarded as a delta-type function when compared to the source time function  $f_L(t)$  of a large tremor. The recorded displacements of the small tremor can be seen as Green

functions. These functions convolute the source time function of the large tremor into the observed displacements of the large tremor, see for example Udias et al. (2014), §6.5<sup>4</sup>.

Figure D.8 shows a few typical apparent source time functions obtained for a few stations around the epicentre, see further Wentinck (2018a). Figure D.9 shows the source time functions of the simulations, following from Eq. (D.3). The duration of the source time functions is of the same order indicating that part of the observed apparent source time function follows from the rupture process along fault dip.

---

<sup>4</sup>Note that the source time function of the small  $M_L$  1.7 tremor is not a pure  $\delta(t)$  function. The method has failed when applying it for other small tremors close to the  $M_L$  3.4 tremor hypocentre. In this respect, the occurrence of the  $M_L$  1.7 tremor was a fortunate coincidence.

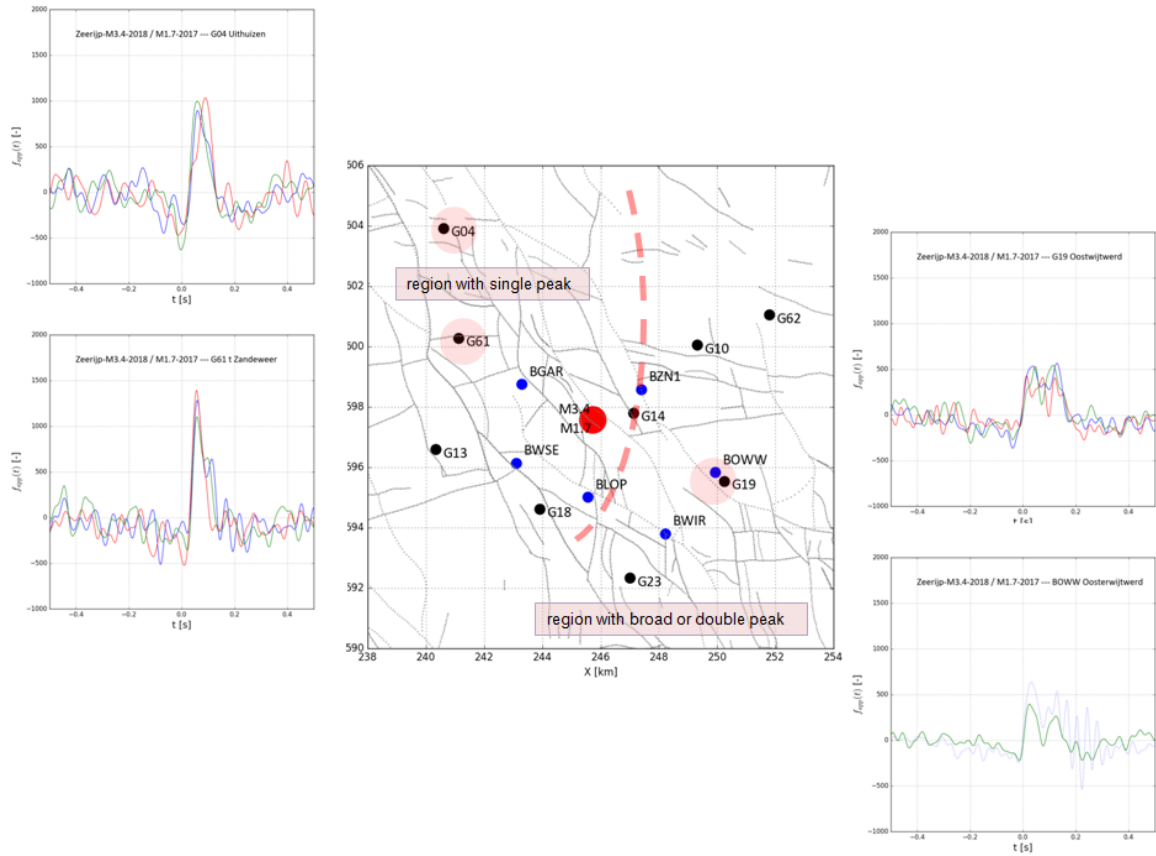


Figure D.8 : Distribution of a few typical apparent source time functions of stations G04, G61, G19 and BOWW around the map from Wentinck (2018a). The sharply shaped source time functions are more to the north west of the Zeerijp tremor epicentre. The broader ones with a double peak are more to the south east of the tremor epicentre.

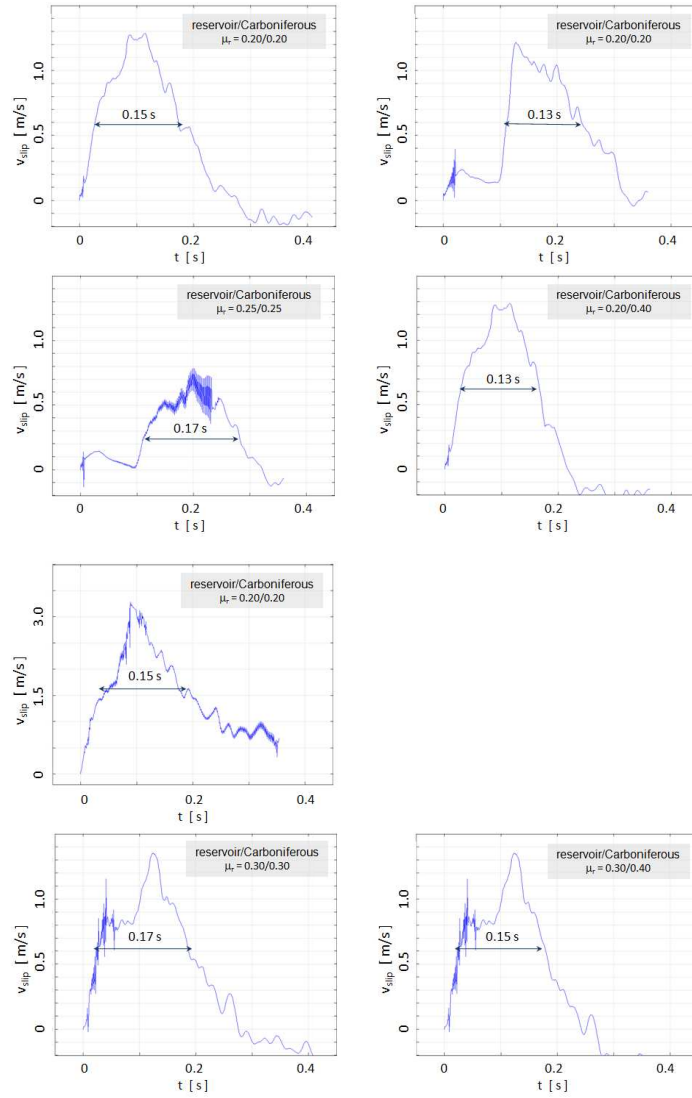


Figure D.9 : Few source time functions derived from simulation A (top 4 figures) and simulation B (bottom 3 figures). The duration of these functions is comparable with those of the observed apparent source time functions shown in Figure D.8 .

## **Appendix D.4 Dynamic rupture simulation in three dimensions**

Natural fault surfaces are curved and rough in three dimensions and surrounded by non-uniform rock. With the current computing capabilities, dynamic rupture modelling of three dimensional faults in a non-uniform compacting reservoir can be done. Figure D.10 shows an example.

The main reason to show this example in this report is that it illustrates connectivity of highly stressed zones along fault strike and how stress may vary along fault strike due to a combination of fault zone curvature and non-uniform rock properties.

Simulations in three dimensions could be useful when fault surface geometries are well constrained and the non-resolved fault curvature or fault roughness is properly included in the parameters for the constitutive models for rock failure. This is a topic of ongoing work.

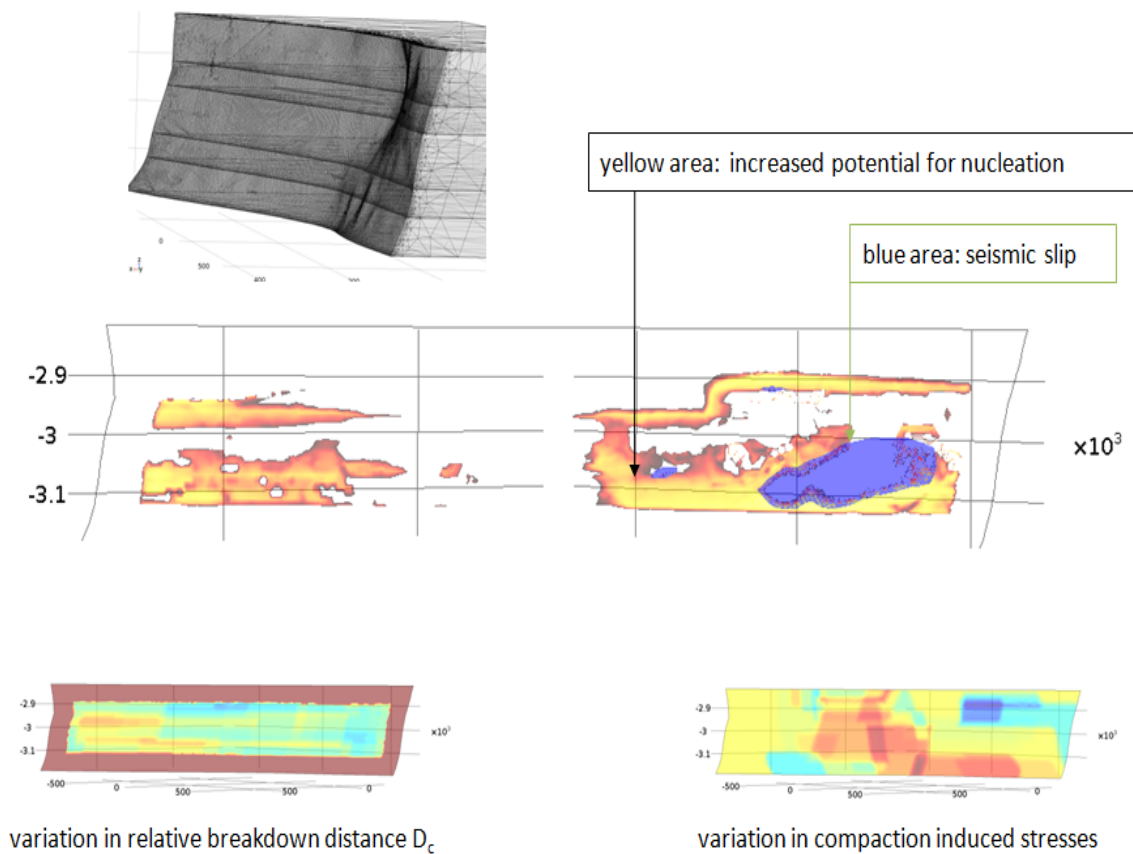


Figure D.10 : Illustration of a simulation of dynamic rupturing in three dimensions. The yellow area shows areas of high stress and brittle rock where nucleation could start. The blue area shows a small rupture plane. To speed up calculations, the grid is refined in and just around the fault zone using boundary layers as shown in the top figure. The grid shown is for the rock of a compacting reservoir, overburden and underburden at one side of the fault zone. The bottom two figures illustrate variations in the compaction induced stress and in the critical breakdown slip  $D_c$ . The variation in the compaction induced stress follows from variations in the uniaxial compaction coefficient  $C_m$ . The variations are expressed by different colours.

Copyright Shell Global Solutions International B.V., Rijswijk International, B.V., 2018.

Neither the whole nor any part of this document may be reproduced, stored in any retrieval system or transmitted in any form or by any means (electronic, mechanical, reprographic, recording or otherwise) without the prior written consent of the copyright owner.